NACA TN 4020

NATIONAL ADVISORY COMMITTEE FOR AERONAUTICS

TECHNICAL NOTE 4020

INVESTIGATION OF MINIMUM DRAG AND MAXIMUM LIFT-DRAG RATIOS OF SEVERAL WING-BODY COMBINATIONS INCLUDING A CAMBERED TRIANGULAR WING AT LOW REYNOLDS NUMBERS AND AT SUPERSONIC SPEEDS

By Clinton E. Brown and L. K. Hargrave

Langley Aeronautical Laboratory
Langley Field, Va.

Washington
September 1958

1A

NATIONAL ADVISORY COMMITTEE FOR AERONAUTICS

TECHNICAL NOTE 4020

INVESTIGATION OF MINIMUM DRAG AND MAXIMUM LIFT-DRAG RATIOS OF SEVERAL WING-BODY COMBINATIONS INCLUDING A CAMBERED TRIANGULAR WING AT LOW REYNOLDS NUMBERS AND AT SUPERSONIC SPEEDS[1]

By Clinton E. Brown and L. K. Hargrave

SUMMARY

Wing-body combinations incorporating several wing plan forms indicated to be of interest from a theoretical analysis were tested at Mach numbers of 1.62, 1.93, and 2.41 in the Langley 9-inch supersonic tunnel. One triangular, one arrow, and two diamond plan forms were tested. The triangular and arrow plan forms were tested with various amounts of camber, which was designed to yield an approximately uniform pressure distribution. Tests of the arrow and triangular wings showed that cambering the surface was an effective way to reduce the leading-edge laminar-separation effects which were present at the low test Reynolds numbers. For the models tested, the laminar separation at the leading edges prevented the possibility of attaining the theoretically predicted leading-edge thrust. The principal conclusions resulting from both the tests and comparison with other available experiments and theory are as follows:

In the Mach number range approaching and beyond 2, the differences in maximum lift-drag ratios between the fully tapered plan forms tested appear to be small and hence the selection of a wing plan form for optimum range will probably depend on factors such as the landing characteristics or control adaptability.

In the same Mach number range, the triangular plan form appears to offer the lowest values of minimum drag and will therefore be of interest for aircraft operating at low lift coefficients.

---

[1]Supersedes declassified NACA Research Memorandum L51E11 by Clinton E. Brown and L. K. Hargrave, 1951.

In the Mach number range below 1.6 it appears that the arrow wing offers the highest maximum lift-drag ratios, although a well-designed, cambered, triangular wing may approach the arrow wing in efficiency and at the same time yield somewhat lower minimum drag values. In particular, the difference in maximum lift-drag ratio will depend on the amount of leading-edge thrust which can be realized in flight, whether the leading-edge thrust is obtained on a rounded or on a cambered leading edge.

INTRODUCTION

The problem of obtaining high maximum lift-drag ratios at supersonic speeds has been discussed by Jones (reference 1) and Puckett and Stewart (reference 2). In both references it is pointed out, insofar as the linear theory can predict, that the highly sweptback arrow wing is superior to other plan forms. In reference 1, it is estimated that a maximum lift-drag ratio of 10.8 could be obtained at a Mach number of 1.41 and a Reynolds number of 10^7 with a reasonable configuration having a highly sweptback wing. In an attempt to obtain experimentally the high lift-drag ratios predicted, Madden (reference 3) conducted tests of a highly swept wing designed for a Mach number of 1.53. The results of the tests indicated that the theoretical lift-drag ratios were not attained because of viscous effects resulting in excessive drag due to lift. In later tests (reference 4) of a cambered wing of reduced thickness-chord ratio, a lift-drag ratio of 9 was obtained at the Mach number 1.53; this result is in better agreement with the theory.

It is apparent from reference 1 that the highly swept arrow wing is theoretically capable of giving the highest maximum lift-drag ratio. Nevertheless, finding the differences in performance between the arrow plan form and others, especially the lift-drag ratios obtainable at lift coefficients below that for maximum lift-drag ratio, is important because the altitudes for flight at the lift coefficient for maximum lift-drag ratio are very high in the supersonic range and, since aircraft will be required to fly at lower altitudes, the lift coefficients will be below the lift coefficient for maximum lift-drag ratio. Also, with modern jet engines, the optimum range occurs at lift coefficients somewhat below the lift coefficient for maximum lift-drag ratio. The present investigation was therefore undertaken to provide information on the lift-drag ratios obtainable from wings of various simple plan forms. The investigation was conducted in two parts: the first part consisted of a theoretical analysis of triangular wings and unswept wings of various taper ratios to determine their lift-drag ratios at all angles of attack; the second part was devoted to tests in the Langley 9-inch supersonic tunnel of the most interesting triangular and

unswept wings selected as being close to the optimum from the results of the theoretical analysis. Upon completion of the triangular-wing tests the models were altered by cutting out the trailing edges to form arrow-type sweptback wings of zero taper ratio. Although the resulting arrow wings were not theoretically predicted optimum wings, the theoretical work indicated that they should yield higher maximum lift-drag ratios than either the triangular or diamond plan forms. In addition to the uncambered-wing models, two triangular and two arrow-type wings were tested, each incorporating camber approximating that for uniform load distribution.

Throughout this paper the word camber is taken to mean a general distortion of the wing surface and hence includes camber and twist as used in the usual sense. The wings were tested on a body of revolution at three supersonic Mach numbers, 1.62, 1.93, and 2.41.

SYMBOLS

A aspect ratio, b^2/S

α free-stream angle of attack, deg

α_{Des} design angle of attack, deg

$\Delta\alpha$ change in angle of attack from value for minimum drag, $\alpha - \alpha_{D_{min}}$, deg

b wing span

$\beta = \sqrt{M^2 - 1}$

c wing chord, measured in direction of flight

$\bar{c}$ mean aerodynamic chord, $\frac{2}{S}\int_0^{b/2} c^2 dy$

C_D drag coefficient, $\frac{\text{Drag}}{qS}$

ΔC_D incremental drag coefficient, $C_D - C_{D_{min}}$

C_{D_f} skin-friction drag coefficient

$C_{D_{min}}$ minimum drag coefficient

C_{D_w} wave drag coefficient

C_L lift coefficient, $\frac{\text{Lift}}{qS}$

$C_{L_{Des}}$ design lift coefficient

$C_{L_{opt}}$ lift coefficient for maximum lift-drag ratio

ΔC_L incremental lift coefficient, $C_L - C_{L_{D_{min}}}$

C_{L_α} lift-curve slope per degree

C_m pitching-moment coefficient, $\frac{\text{Moment about center of area}}{qS\bar{c}}$

$\Delta C_m = C_m - C_{m_{l_0}}$

C_{m_α} pitching-moment-curve slope per degree

E complete elliptic integral of the second kind

F_s theoretical leading-edge suction-force coefficient,

$$\frac{\left(C_L - C_{L_{Des}}\right)^2\sqrt{1 - m^2}}{4\pi \cot \Lambda_{LE}}$$

j location of center of wing area from apex of fuselage, percent of fuselage length

k location of maximum airfoil thickness measured from leading edge in streamwise direction, percent chord

L/D lift-drag ratio

$(L/D)_{max}$ maximum lift-drag ratio

l fuselage length

$m = \beta \cot \Lambda_{LE}$

M stream Mach number

q dynamic pressure, $\frac{\rho V^2}{2}$

ρ stream density

R Reynolds numbers based on mean aerodynamic chord

r_o maximum radius of fuselage, in.

S wing plan-form area including the area obtained by extending the wing leading and trailing edges to the fuselage center line

t maximum wing-section thickness

V free-stream velocity

W/S wing loading

Λ_{LE} sweep angle of leading edge, deg

Λ_{TE} sweep angle of trailing edge, deg

x coordinate along free-stream direction

y lateral (spanwise) coordinate

z vertical coordinate of wing camber line

Subscripts:

r value at root section

t value at tip section

D_{min} value at minimum drag

l_0 value at zero lift

ANALYSIS

In level flight the thrust of an aircraft is proportional to the weight and inversely proportional to the lift-drag ratio; hence it is always desirable to obtain high values of the lift-drag ratio. In flight, operation of the aircraft at the incidence of maximum lift-drag ratio seems desirable. The lift produced at this incidence, however, must equal the aircraft weight and therefore a certain restriction on either wing loading, altitude, or speed is imposed. Fixing the wing loading and lift coefficient thus yields a relation between flight altitude and Mach number for a standard atmosphere. This relation for several values of lift coefficient and wing loading is shown in figure 1.

The curves clearly illustrate that, for reasonable wing loadings, a supersonic airplane or missile must go to extreme altitudes to fly at the lift coefficient for maximum lift-drag ratio. (A value of $C_{L_{opt}}$ of 0.20 is considered typical.) As tactical aircraft may be required to fly at low altitudes, investigation of the lift-drag ratio problem at low lift coefficients is important. At vanishing lift coefficients the lift-drag ratio depends primarily on $C_{D_{min}}$ as can be seen from the following equation for uncambered wings:

$$\frac{L}{D} = \frac{C_L}{C_{D_{min}} + KC_L^2} = \frac{C_L}{C_{D_{min}}}\left(1 - \frac{KC_L^2}{C_{D_{min}} + KC_L^2}\right)$$

where K is the drag-rise factor dC_D/dC_L^2. The minimum drag coefficient is therefore the important design parameter for performance of low-altitude supersonic aircraft; whereas the maximum lift-drag ratio is the most important for high-altitude aircraft. It is clear, of course, that, for aircraft operating over wide speed and altitude ranges, consideration of both parameters must be made to insure the highest lift-drag ratios at values of lift coefficient between zero and $C_{L_{opt}}$.

The effects of wing plan form on these parameters can be estimated by using the results of the linearized theory of supersonic flows together with suitable skin-friction factors and certain simplified structural criteria. It is convenient for comparison of results to extend the work of Jones (reference 1) on swept plan forms to other plan forms of interest. Therefore, the analysis is carried out by using the same fuselage shape, relative wing area, skin-friction factors, and structural criteria as were used by Jones. A brief summary of the assumptions follows: the

ratio of wing area to fuselage frontal area was set at 25; the wing minimum drag was increased by 10 percent to account for a tail surface; the fuselage had a fineness ratio of 12.5 and was a shape calculated to give a minimum drag for a given volume and length; the design Reynolds number was assumed to be 10^7; and the wing thickness at the root was chosen to be one-fifteenth the distance along the maximum thickness line to the wing centroid of area. This last assumption, of course, introduces a dependence of the thickness drag upon the plan form and tends to penalize the high aspect ratios as should be the case. It is realized, however, that the important effects of wing stiffness and weight are not taken into account and, therefore, the structural criterion used should be regarded as a first approximation. For the computations, the values of lift-curve slopes were obtained from references 5 to 7. The zero-lift pressure-drag coefficients were obtained in the same manner as those of reference 1; that is, the coefficients were determined for wedge-type profiles and increased by one-third to allow for a section shape of higher strength. The maximum thickness line for the triangular wings was chosen at the 30-percent-chord line since the results of reference 8 indicate a lower wave drag for wedge-type sections with the maximum thickness well forward of the midchord position when the leading edge is swept behind the Mach cone. The maximum thickness line for the unswept tapered wings was fixed at the midchord line, the same as for the arrow wings. The values of the wedge-section drag coefficients were obtained from references 8 to 10. The drag due to lift for the unswept tapered wings was taken as the lift times the angle of attack; whereas the drag due to lift for the triangular and arrow wings was obtained from references 1 and 5. Incompressible, turbulent-boundary-layer, skin-friction factors were assumed for wing and fuselage and the effects of angle of attack on skin-friction factors were neglected. The drag of the isolated wing was added to the fuselage drag; the conservative error in this case was intended to allow for some adverse interference effects. The results of the present analysis at $M = 1.41$ for uncambered triangular and unswept wings of three taper ratios are presented in figures 2 and 3 with the results of arrow wings from reference 1.

The arrow wings of reference 1 have a fixed trailing-edge sweepback angle equal to the Mach angle so that the aspect-ratio variation results in a change of leading-edge sweepback. The tapered unswept wings were symmetrical lengthwise so that the leading-edge sweepback was equal to the trailing-edge sweepforward.

The variation of minimum drag coefficient with aspect ratio (fig. 2) shows that for each plan form the lower aspect ratios are best. At the lower aspect ratios there is little difference between the arrow, triangular, and diamond plan forms, and from this limited analysis it appears that the choice of plan form will be dictated by other considerations. From the standpoint of maximum lift-drag ratio, however, figure 3

indicated that the arrow wing is superior to the triangular and unswept wings for a large range of aspect ratios and that it is indeed the most promising plan form for efficient supersonic flight if the theoretical results can be approached in flight. Unfortunately most available data indicates that only a portion of the theoretically predicted leading-edge suction force has been obtained. Since the drag relief produced by the leading-edge suction is quite important in obtaining high lift-drag ratios on both the arrow and triangular wings, curves at $(L/D)_{max}$ have been plotted for which only one-half the leading-edge suction force was assumed. These curves show that the arrow wing, triangular wing, and diamond wing would all produce about the same maximum values of $(L/D)_{max}$.

It should be remembered that the concept of leading-edge thrust arises in linearized theory and is not a clearly defineable physical quantity. When linear theory is compared with the experimental results the leading-edge thrust will be burdened with other effects such as the viscous drag due to lift, eddy drag at trailing edges, and possibly the drag associated with shock formation not predicted in linear theory. The leading-edge thrust as used is only a concept useful in establishing a base for comparisons.

The uncambered triangular and arrow wings at an angle of attack are known to have pressure distributions similar to subsonic airfoils; that is, there is a low-pressure region on the leading edge followed by a very rapid increase in pressure. These pressure gradients are unfavorable to smooth boundary-layer flow and quickly produce transition from laminar flow to turbulent flow or more often, at low Reynolds numbers, produce flow separation. (See reference 3.) In addition it is known that, under certain conditions of Mach number and angle of attack, shock waves form on the upper surface of the wing causing separation and deviation of the flow from that predicted by means of the linear theory. As the effects just discussed were anticipated for the flat triangular and arrow wing plan forms, the test program was enlarged to include cambered triangular and arrow wings. As a first step, it was decided to investigate camber for approximately uniform loading at two design lift coefficients. The equation for the camber surface for a uniformly loaded triangular wing was obtained from reference 1 and is

$$z = \frac{\beta C_L}{4\pi m}\left\{\frac{\sqrt{1 - m^2}}{m}\left[(\beta y + mx)\cosh^{-1}\frac{x + m\beta y}{|\beta y + mx|} - (\beta y - mx)\cosh^{-1}\frac{x - m\beta y}{|\beta y - mx|}\right] - 2\left(x\cosh^{-1}\frac{x}{|\beta y|} - \sqrt{x^2 - \beta^2 y^2}\right)\right\}$$

where $\beta = \sqrt{M^2 - 1}$ and $m = \beta \cot \Lambda_{LE}$. The infinite ordinates at the root sections produce a camber surface which is, of course, impossible to construct so the camber distribution was modified near the root section. The modified camber surface will not yield a uniform loading; however, it was felt that the alteration would not affect to any reasonable degree the smoothness of the pressure distribution near the leading edges.

As the lowest available test Mach number in the Langley 9-inch supersonic tunnel was 1.62, the wings were selected from curves similar to those in figures 2 and 3 but were prepared for the Mach number 1.62. However, the curves for $M = 1.62$ are not shown as there are only small differences between the two Mach numbers.

Since $(L/D)_{max}$ for the triangular wing varies little with aspect ratio near the optimum, the aspect ratio chosen was somewhat smaller than the optimum in order to obtain a smaller $C_{D_{min}}$. The fully tapered wing appeared to be the best choice for the unswept plan form; therefore, two diamond wings of aspect ratio 2.5 and 3.5 were selected for testing. These two aspect ratios are both close to the theoretical optimum for $(L/D)_{max}$.

The actual test models varied somewhat from the models of the theoretical treatment. The section thickness ratios were increased outboard of the root section to allow for greater wing stiffness; the wing areas were also revised so that the ratio of external wing area to fuselage frontal area was constant at approximately 23 for all configurations.

APPARATUS AND TEST PROCEDURE

Wind Tunnel and Model Support

The investigation was conducted in the Langley 9-inch supersonic tunnel, a brief description of which can be found in reference 11.

All of the wing-fuselage combinations were mounted from the rear of the fuselage as shown in figure 4. The model forces are transmitted to the balance system by the sting and sting-supporting bars which are shielded from the tunnel air stream by a partially movable windshield. An angle-of-attack mechanism pivots the sting support and movable windshield about a point at the juncture of the movable and fixed windshields and allows the model to be set at angles of attack up to about $\pm 10^{\circ}$. To prevent the flow of air over the sting and sting support, the clearance

at the model base between the model and the movable windshield was held at about 0.005 inch and a flexible rubber boot was slipped over the juncture of the movable and fixed windshield. The scales are self-balancing beam scales and measure three components, in a horizontal plane, of the total forces on the model and support system.

Models

The fuselage shape used has been determined by Haack (reference 12) to have the minimum pressure drag for a given length and volume if closure at the tail is assumed as shown in figure 5 by the dashed lines. The rear of the fuselage was cut off to permit installation in the balance-support system and is assumed to represent a typical fuselage with a jet exit. Four mild-steel fuselages were constructed. Three of these bodies had a maximum diameter of 0.760 inch corresponding to a frontal area 0.0432 times the external area of the diamond and triangular plan-form wings. The fourth fuselage had a maximum diameter of 0.591 inch corresponding to a frontal area 0.0414 times the external area of the arrow plan-form wings. One of the large fuselages was made with a hollow support to permit installation of four pressure orifices in the base of the body so that the fluctuations of base pressure with gap size and alinement of the movable windshield could be determined. The other two large bodies had solid supports and were constructed to permit installation of the triangular and diamond wings of two different incidences with respect to the fuselage center line, 0° and 3°. The small fuselage was constructed to permit installation of the arrow wings at 0° incidence. A small mirror flush-mounted near the rear of each body was used with an optical angle-of-attack system to measure the angle of attack of the fuselage during the tests.

The diamond plan-form wings have circular-arc streamwise sections, the $A = 2.5$ wing having a thickness ratio of 1.4 percent at the root section and the $A = 3.5$ wing having a thickness ratio of 2.0 percent at the root section. The thickness ratios for all wings vary spanwise as shown by the curve in figure 6(a). Both diamond wings were mounted in the fuselage with their center of area 4.650 inches from the nose of the fuselage.

Three wings of triangular plan form were tested: one uncambered, one cambered to give approximately uniform load at $C_L = 0.08$ and $M = 1.62$, and the other cambered to give approximately uniform load at $C_L = 0.20$ and $M = 1.62$. All triangular wings have an NACA 0002 root airfoil section which has its maximum thickness at 30 percent of the chord. The leading-edge radii were modified to give a smooth contour at the nose and average about 0.2 percent of the local chord. The triangular wings were mounted in the fuselage with the center of area of the wing 5.875 inches from the nose of the body.

The spanwise camber lines of the cambered triangular wings are shown in figure 6(b). Since each camber surface is composed of straight-line elements passing through the wing apex, it can be described graphically by sections taken normal to the flight direction, each section being similar but of a scale increasing linearly in the downstream direction. Therefore, the two spanwise camber lines specify both camber surfaces. Since the theoretical camber surfaces would give the root-section chord line infinite ordinates, they were modified by drawing tangents to the spanwise camber lines at $\frac{y}{x} = 0.106$ as shown by the dashed portions of the curves in figure 6(b). Most of the modified area is contained within the fuselage. These modifications gave, at the root chord lines, angles of attack of 2.85° at the design lift condition for the $C_{L_{Des}} = 0.08$ cambered wing and 7.08° at the design lift condition for the $C_{L_{Des}} = 0.20$ cambered wing.

The cambered triangular wings were tested in two identical fuselages with the section at the wing-body juncture at approximately 0° incidence for one case and 3° incidence for the other case. A photograph of the $C_{L_{Des}} = 0.20$ cambered triangular wing on the body at 0° incidence is shown in figure 7. The resulting fuselage angles of attack for which the wings are at their design condition are given in the following table. These are the theoretical values and only apply at $M = 1.62$.

Wing	Fuselage angles of attack	
	0° incidence	3° incidence
$C_{L_{Des}} = 0.08$ triangular wing	2.47	-0.53
$C_{L_{Des}} = 0.20$ triangular wing	6.18	3.18

The arrow plan-form wings were made by cutting out the rear of the triangular wings along a 45° line to form fully tapered arrow wings of aspect ratio 2.57. The sections were modified by forming a linear variation of thickness from the maximum thickness line to the trailing edge. The intersection of the 45° cutoff line with the camber surface was used as the trailing edge so that the camber surface of the wing was unchanged. The discontinuity in slope at the maximum thickness line was faired into the wing surface to form a smooth curve. The thickness ratio of the root section with these modifications was 3.3 percent.

The geometric properites of all wings are summarized in table I. Sketches of the various wing and fuselage combinations are shown in figure 5. All of the wings and fuselages were hand-polished. For all tests of the wing-fuselage configuration, the wing-body juncture and bolt holes were filled with plaster and faired to the fuselage shape.

Test Procedure and Precision

Three component data were taken through an angle-of-attack range and reduced to give lift, drag, and pitching moment. Schlieren planform photographs were taken for most configurations to determine the shock-wave pattern. The liquid-film technique as described in reference 11 was used to determine the nature of the boundary-layer flow on most configurations. The models were given a black finish before applying the liquid-film solution. Upon completion of a test run, the models were dusted with white powder. Accordingly, the wet regions appear white in the photographs and the dry regions remain black.

A correction to the drag was applied to account for the difference between free-stream pressure and the sting-shield-and-balance-enclosing-box pressure. The base-pressure measurements showed that this box pressure acted over the entire base area at least for the variation in box pressure and misalinements of the movable windshield which were experienced during the tests. The corrected drag values for the wing-fuselage configuration corresponds approximately to those for a power-on aircraft with a jet in the rear of the fuselage with pressure $P_{exit} \cong P_{stream}$. Therefore, if this condition is not met, the results should be corrected to account for the base drag effects. On the $C_{L_{Des}} = 0.20$ cambered triangular wing on a sting model, the effect of the sting on the combination is negligible. (See reference 11.)

The estimated probable error in the measured aerodynamic quantities based on the smallest wing area and dynamic pressure are as follows:

C_L	±0.00015
C_D	±0.00015
C_m	±0.00020

These are the errors at any specified angle of attack and Mach number. The probable error in angle of attack is $\pm 0.08^\circ$ in the initial reference of each configuration with respect to the tunnel walls and 0.01° in relative angle of attack. Stream surveys indicate that the maximum deviation of the local-stream direction from the tunnel center line is not more than 0.25°. In addition, there is some error introduced in

mounting the wing in the fuselage which may be as large as 0.2°. The probable error in Mach number is ±0.01.

Tests Results

The variations of lift, drag, and pitching-moment coefficients with angle of attack for the fuselage alone at $M = 1.62$ is shown in figure 8. There were only negligible differences in the aerodynamic characteristics of the large and small fuselages tested. The coefficients are based on the frontal area and length of the fuselage. The pitching moment is taken about the maximum diameter of the fuselage, a point 4.760 inches from the nose of the large body.

Figure 9 compares the experimental curves of C_{L_α}, C_{m_α}, and $C_{D_{min}}$ against Mach number with the theoretical values calculated by the methods of Von Kármán and Moore (reference 13) and Lighthill (reference 14). The values of $C_{D_{min}}$ were obtained by adding an incompressible, laminar, friction drag coefficient to the wave drag calculated by the Von Kármán-Moore method. The theoretical values of C_{L_α} and C_{m_α} were obtained by Lighthill's method.

The variation of C_L, C_D, C_m, and L/D with angle of attack for wing-body configurations at $M = 1.62$ are shown in figures 10 to 18. All coefficients are based on the area and mean aerodynamic chord of the wing in that particular configuration, and the pitching moments are taken about the centroid of wing area. The theoretical lift-curve of the wing alone is also shown for comparison. The theoretical curves are shown by dashed lines and are drawn through the experimental zero-lift point for all except the uncambered wings on the zero-incidence bodies. The design angle of attack of all cambered-wing configurations is shown by dashed lines. The values of $(L/D)_{max}$, $C_{D_{min}}$, C_{L_α}, and $C_{L_{opt}}$ for all configurations tested are summarized in table II.

DISCUSSION OF RESULTS

Minimum drag.- A summary of minimum drag values for the various test models is given in figure 19. As anticipated the minimim drag values for the cambered wings were higher than those of the corresponding flat wings and the drag due to camber varied approximately as the square of design lift coefficient. The triangular wing produced the lowest values of $C_{D_{min}}$ even though its thickness ratio was somewhat greater than that of the diamond wing. A comparison of calculated and

experimental values and liquid-film studies made on the triangular-wing configuration indicates that wing-body interference is responsible for the rather large variation of minimum drag with Mach number. To illustrate this conclusion a drag breakdown is given in figure 20 in which the experimental data are plotted with the calculated drag components. In this breakdown, the wings are assumed to have a full laminar boundary layer, whereas both laminar and turbulent friction factors are used and given for the fuselage friction drag. Actually, the turbulent flow when it occurs is concentrated on both the body and wing near the wing-body junction; hence the calculation simply allows an orientation of the experimental drag values. In figure 20 comparison of experiment and theory indicates that for both the arrow and the triangular wings at $M = 1.62$ there is a large amount of turbulent flow which is reduced as the Mach number increases. The liquid-film pictures of figure 21 show this effect to be true since the model shown at $M = 1.62$ obviously has a large amount of scrubbed area near the wing body juncture; whereas the picture shown at $M = 2.40$ seems to indicate that the flow remains laminar even close to the body-wing juncture. The trend of the $A = 2.5$ diamond wing experimental values is similar to those of arrow and triangular wings except that the turbulent flow appears to persist to the highest Mach numbers. It was not possible to determine whether or not there was actually a large region of turbulent flow in the region of the wing-body junctures because the liquid-film photographs for this wing were extremely poor. It is possible, of course, that the perfect-flow (inviscid) wing-body interference for the diamond-wing configuration is somewhat greater than that of the highly sweptback wing configurations.

In order to obtain a better wave-drag estimate than was used in the analysis section, the theoretical wave drag for the round-nosed airfoil sections used on the test wings was estimated by approximating the true airfoil sections by several straight-line segments. The substitute wing used for the calculations was assumed to be of constant thickness ratio; whereas, for the test wings, the thickness ratio varied. The value of the thickness ratio for the substitute wings, therefore, was taken to be the thickness ratio of the mean aerodynamic chord for the test wings. It was found that a considerable change in drag can be calculated when changing from double wedge to other airfoil shapes. The change can be either positive or negative depending on the particular conditions of Mach number, sweep of leading edge, and so forth. Figure 22 shows some computed values for the three wing plan forms of the tests. It is probable that all the values obtained near the Mach numbers at which the flow component normal to the lines of discontinuous slope becomes sonic are in error since the linearized theory cannot reasonably be expected to describe the flow under these conditions. The blunting of the nose sections for the triangular and arrow plan forms does not cause a very large increase in the calculated drag and the increase of 33 percent assumed in the analysis is excessive. In fact the results indicate that,

for a small range of Mach numbers for the arrow wing, a reduction in drag may result. It is reasoned that the effect is greater for the arrow wing than for the triangular wing because the double-wedge arrow wing has its maximum thickness at 50 percent of the chord and the blunting effectively shifts the centroid of section area forward. The shift of section area forward should tend to reduce the drag in light of Puckett's work (reference 8) in which it is shown that the drag is generally least for forward positions of maximum thickness of double-wedge airfoil sections when the leading edge is well behind the Mach line. The diamond wings seem to follow the estimated 33-percent drag increase fairly well and hence the results of the analysis in this respect should be reasonably accurate.

The triangular-wing models which showed considerable turbulence in the wing juncture were tested with fillets in an attempt to improve the flow; however, since the fillet increased the total frontal area of the model, no conclusions could be made from the force tests. Nevertheless, liquid-film studies showed no appreciable decrease in the turbulent areas and it was concluded that the fillets were of little value.

Lift-curve slope.- The theoretical and experimental lift-curve slopes for the body alone are shown in figure 9. The theoretical value is considerably lower than the experimental values taken through the zero lift points. The reasons for the discrepancy are not entirely clear; however, it appears from the experimental pressure studies of reference 15 that separation or at least severe boundary-layer thickening occurs on the top portions of the body even at very low angles of attack. Allen's theory (reference 16) predicts such a behavior but is really of quantitative value at large angles of attack only where the viscous effects dominate the flow. It is probable that the lift-curve slopes near zero lift would be in better agreement with linear theory if the models were tested at higher Reynolds numbers where the boundary layers are turbulent.

The lift curves for the wing-body configurations at $M = 1.62$ are presented in figures 10 to 18 together with the theoretical curves computed for the wings alone. In figure 23, the lift-curve slopes taken over a lift-coefficient range from zero to 0.15 are plotted against Mach number. The closest agreement between theory and experiment was obtained with the diamond plan form for which the leading edges were always supersonic. The triangular wings gave very good agreement at $M = 1.62$, but fell below theory as the Mach cone of the flow approached the leading edge. This Mach cone effect was evident for the diamond and arrow wings as well. The arrow wings yielded a smaller percentage of the theoretical lift, an effect which might be expected since the steeper trailing-edge angles of the arrow wing sections would tend to produce a greater extent of trailing-edge separation.

Center-of-pressure positions.- A plot of the center-of-pressure position against Mach number for two values of C_L is given in figure 24 for the diamond-, triangular-, and arrow-wing configurations. As can be seen, there is very little change in center-of-pressure position with Mach number within the lift-coefficient range of 0.05 and 0.15. These curves were computed from the following equation:

$$\text{Center-of-pressure position} = \frac{\Delta C_m}{C_L}$$

where

$$\Delta C_m = C_m - C_{m_{l_0}}$$

This procedure removes the theoretically constant zero-lift moment due to intentional and unintentional camber; hence the center-of-pressure positions for the cambered wings are fictitious and are only presented to allow a simple comparison with the theory. The theoretical triangular-wing-alone center-of-pressure position is always at the center of wing area since the camber surface is a conical sheet. The low Reynolds numbers of the tests with the attendant laminar-flow separation effects previously mentioned make a detailed discussion of the center-of-pressure travel rather useless. The tests, however, do indicate that center-of-pressure travel of all configurations is of a much lower order than that anticipated in flying from a subsonic speed to a supersonic speed.

Drag due to lift.- The linearized theory predicts a leading-edge thrust for wings having their leading edges behind the Mach cone from the wing apex. (See reference 5.) This thrust is an important factor in reducing the drag due to lift and therefore contributes considerably to the maximum lift-drag ratio. Unfortunately, the present data for the triangular and arrow wings indicate that very little of this leading-edge thrust is obtained. To show this effect clearly, figures 25(a), 25(b), and 25(c) in which the curves are drawn representing the drag to be expected with and without leading-edge suction force have been prepared. The long-dash—short-dash line is simply the product of ΔC_L and $\Delta\alpha$. The drag including the suction force was obtained by subtracting the theoretical values of suction-force coefficient F_s from the experimental values of $(\Delta C_L)(\Delta\alpha)$. The plots for the uncambered arrow and triangular wings indicate a rapid drag rise with lift coefficient near zero lift, but at higher angles the slopes of the experimental drag curve and the curve for $(\Delta C_L)(\Delta\alpha)$ were about equal. It should be emphasized that the comparison of the slopes of the actual data curves with the theoretical curves can indicate the amount of leading-edge thrust obtained only when the viscous drag is constant with angle of attack. The cause of the rise in drag at low lift coefficients is the onset of separation from the leading edge

of the wing. For the very thin wings tested, the flow over nearly the entire leading edge appears to become separated at angles of attack of 2° or more. Photographs of the wing flow pattern obtained by use of the liquid-film method show the leading-edge separation quite clearly. Figure 26 shows the upper and lower surface of the flat triangular wing at $M = 1.62$ and $\alpha = 4.5^{\circ}$; the liquid film has been dusted with powder so that the dark regions indicate dried portions. On the upper surface the leading-edge region is white and indicates a complete flow separation, whereas the dark regions following indicate the point of flow reattachment with the resultant high surface shear tending to scrub off the liquid film. The lower surface indicates a typical pattern for laminar flow; the dark leading edges are a result of the high surface shear at the beginning of the laminar layer, whereas the dark regions adjacent to the body are regions of turbulence produced by wing-body interference. The effect of increased Reynolds number on the separation cannot be predicted at this time; however, as the Reynolds number or the leading-edge radius is increased, the fraction of leading edge which is separated probably will decrease. It is doubtful that, for the thin wings necessary for efficient flight, the leading-edge separation can be completely eliminated even at high Reynolds numbers without the use of camber. The camber would, of course, only prevent the separation near the design angle of attack.

The drag plots for the cambered wings (figs. 25(b) and 25(c)) indicate a small amount of suction force over the low lift-coefficient range at $M = 1.62$. This effect, however, is the result of the improved boundary-layer flow as the wing approaches its design point and is not the result of any leading-edge-suction phenomenon. At zero lift the cambered wings produce a region of separated flow on the lower surface and a loss in leading-edge suction and thus a rather large minimum drag value results; as the lift coefficient increases, the flow separation disappears and hence the apparent drag relief. The leading-edge separation which occurs near minimum drag is clearly shown in the liquid-film picture of figure 27. It should be noticed that the separation occurs on the lower surface. Near and above design lift conditions the drag curve appears to become parallel to the curve computed on the basis of no leading-edge suction.

The general conclusion can be drawn that, for the tests at low Reynolds numbers presented herein, the presence of leading-edge flow separation prevents the attainment of the leading-edge suction forces predicted by linear theory.

The favorable effect of camber on the boundary-layer flow over the triangular wings can be seen in figure 28 where both upper and lower surfaces show a typical laminar flow pattern (compare with fig. 21).

Since the theory predicts no leading-edge forces for wings with supersonic leading edges, only the curve for $(\Delta C_L)(\Delta\alpha)$ for the diamond wing is shown (fig. 25(a)). The experimental incremental drag values, however, were slightly higher than that obtained from $(\Delta C_L)(\Delta\alpha)$. This result may be produced by wing-body interference or boundary-layer and separation effects. If these same effects are present in the triangular- and arrow-wing results it would indicate that more leading-edge suction is present than is indicated in the figures.

Lift-drag ratios.- A summary plot of values of maximum lift-drag ratio is given in figure 29. In this figure is also plotted the results of the tests on two 63° sweptback wings with the same fuselage as that of the present investigation (references 17 and 18). One of these wings was uncambered and had a thickness of 4.54 percent while the thickness of the cambered wing was 5 percent. The sweptback wings were designed for a Mach number of 1.53; whereas the wings of the present tests were designed for a Mach number of 1.62. The ratio of wing area to fuselage frontal area for the 63° sweptback wing configurations was somewhat smaller than those of the present tests. The thickness of the wings used in the tests was somewhat greater than that which would be calculated from the simplified structural criterion used in the analysis, whereas the wings of references 17 and 18 are somewhat too thin. Thus, a comparison of the values of $(L/D)_{max}$ obtained in the investigations must be made with care. Near a Mach number of 1.6, the data for the cambered 63° sweptback wing are slightly higher than the best results of the present tests. It is apparent that the 63° sweptback configuration is definitely superior to those reported herein at the lower Mach numbers. It is possible, of course, that the performance of triangular and diamond wings could be improved at the lower Mach numbers by reducing the sweepback. The value of $(L/D)_{max}$ of 12.9 obtained in reference 17 at $M = 1.2$ is certainly an encouraging result for a supersonic airplane.

The curves of figure 29 indicate that for the wind-tunnel test conditions the cambered triangular wings and the diamond wing yield values of $(L/D)_{max}$ which are nearly equal over the test Mach number range. The $C_{L_{Des}} = 0.20$ arrow wing gave a maximum value of 8 at $M = 1.62$ but showed a greater reduction with Mach number than the triangular and diamond wings. The poor results obtained for the uncambered arrow and uncambered triangular wings are unquestionably the effect of leading-edge separation. The important question which arises is, of course, whether a substantial increase in Reynolds number would improve the flat-wing results. The results of the tests of references 17 and 18 at reasonably high Reynolds numbers seem to indicate that the improvement would be small. This conclusion must certainly be true for sharp leading edges and even rounded edges on very thin wings. As the

Reynolds number is increased and the leading edges are modified to give most rounding at the needed points of the leading edge it is possible that more leading-edge thrust can be obtained. The ability to design the leading edge correctly would indeed be desirable since it would allow a smaller design lift coefficient for the camber and thereby result in reduced minimum drag values. The general reduction of $(L/D)_{max}$ with Mach number is primarily the result of the diminishing lift-curve slopes.

That definite improvement in $(L/D)_{max}$ is obtained by the use of camber can be better seen and understood by detailed comparison of theory and experiment. In figures 30(a), 30(b), and 30(c) there are presented curves of experimental lift-drag ratio against lift coefficient and, for the flat wings and triangular cambered wings at $M = 1.62$, the theoretical curves have been drawn. In figure 31 the theoretical and experimental curves for the triangular wings at $M = 1.62$ have been collected on one sheet to provide an easier comparison between flat and cambered wings.

The theoretical curves for the flat wings were computed by using the experimental minimum drag values for the wing-body configuration and the linearized theory result for drag due to lift. The triangular-cambered-wing curves were computed by using the following equations[1]:

$$C_D = C_{D_{min}} + \frac{K_1}{C_{L_\alpha}}\left(\Delta C_L\right)^2$$

$$\left(C_L\right)_{D_{min}} = C_{L_{Des}}\left(1 - \frac{1 + K_3 C_{L_\alpha}}{2K_1}\right)$$

where K_1 represents the ratio of the theoretical drag due to lift of a flat triangular wing to the drag without leading-edge suction C_{L_α}; and $C_{D_{min}}$ is computed as the sum of the experimental $C_{D_{min}}$ for the flat triangular wing-body configuration and the theoretical drag due to camber at minimum drag C_{D_c} given by the following expression:

$$C_{D_c} = C_{L_{Des}}{}^2\left[K_2 - \frac{\left(1 + K_3 C_{L_\alpha}\right)^2}{4C_{L_\alpha} K_1}\right]$$

---

[1] Note that for these equations C_{L_α} is expressed in units per radian.

where

$$K_1 = \left[1 - \frac{\sqrt{1 - m^2}}{2E\sqrt{1 - m^2}} \right]$$

$$K_2 = \frac{\beta}{2\pi m} \left[\cosh^{-1} \frac{1}{m} + m \sin^{-1} m + \sqrt{1 - m^2} \log_e m \right]$$

$$\frac{K_3}{\beta} = \frac{1 - \sqrt{1 - m^2}}{2\pi m} \log_e \frac{m}{2} + \frac{\sqrt{1 - m^2}}{\pi^2 m} \int_0^{m/2} \log_e \left(\sqrt{1 - m^2} + \sqrt{1 - m^2 \sin^2 x} \right) dx -$$

$$\frac{1}{\pi^2 m} \int_0^{m/2} \log_e \left(1 + \sqrt{1 - m^2 \sin^2 x} \right) dx$$

The integrations indicated in the expression for K_3 have been performed mechanically and the value of K_3/β as a function of m is presented in figure 32. The equations presented are valid for a fixed wing at its design Mach number only since the camber surface provides the uniform loading only at its design Mach number.

It is apparent from inspection of the curves that the flat triangular wing and especially the flat arrow wing suffer seriously from loss of the leading-edge thrust. On the other hand the cambered triangular wings appear to approach more closely their calculated design lift-drag ratios. Again, however, the failure to obtain the leading-edge suction prevents the cambered wings from maintaining the theoretical trend above the design lift coefficient. This effect is particularly noticeable for the $C_{L_{Des}} = 0.08$ triangular wing for which a sharp topping of the lift-drag-ratio curve occurs near a lift coefficient of 0.10 where separation occurs on the leading edges. The camber-wing results at lift coefficients below $C_{L_{opt}}$ appear to be slightly higher than the theoretical. This effect is most pronounced for the $C_{L_{Des}} = 0.20$ triangular wing and is caused by the modification of the actual wing camber surface from that of the theoretical uniform load camber; thus, the modified camber surface having

smaller section slopes near the root yields a somewhat lower minimum drag coefficient and hence better lift-drag ratios at low lift coefficients. The theoretical curves of figure 31 show that the uniform-loading camber is not optimum since at the design lift coefficient the cambered wings yield L/D values almost halfway between the flat wings with and without the attainment of a leading-edge thrust. The more optimum camber surface would be one which prevents separation and reduces the possibility of shock waves by reducing the peak pressures on the leading edge but at the same time approaches the theoretical drag due to lift of the flat wings. It is probable that this optimum camber surface could be attained by striving for span loadings which are only slightly different from the elliptic. The possibility that shocks can occur on triangular wings was shown in reference 11. The phenomenon is similar to that experienced on two-dimensional wings at high subsonic speeds. (See reference 19.) The use of camber can eliminate such shocks by relieving the peak pressures forward at the leading edge of uncambered wings and thus effectively increase what might be called the supersonic critical speed of the triangular wing.

The data obtained show little effect of wing incidence on $(L/D)_{max}$, at least within the range from 0° to 3°.

The $A = 2.5$ diamond plan-form wing can be seen to offer some interest in that it yielded values of lift-drag ratios over the entire lift-coefficient range which were the same as those of the $C_{L_{Des}} = 0.08$ triangular wing. It is only less interesting than the triangular wing because the latter seems to offer more chance for improvement. In addition the triangular wing appears to offer better stability performance in the transonic range.

CONCLUSIONS

Wing-body combinations incorporating several wing plan forms indicated to be of interest from a theoretical analysis were tested at Mach numbers of 1.62, 1.93, and 2.41 in the Langley 9-inch supersonic tunnel. One triangular, one arrow, and two diamond plan forms were tested. The triangular and arrow plan forms were tested with various amounts of camber, which was designed to yield an approximately uniform load distribution. Tests of the arrow and triangular wings showed that cambering the surface was an effective way to reduce the leading-edge laminar-separation effects which were present at the low test Reynolds numbers. For the models tested, the laminar separation at the leading edges prevented the possibility of attaining the theoretically predicted leading-edge thrust. The principal conclusions resulting from

both the tests and comparison with other available experiments and theory are as follows:

1. In the Mach number range approaching and beyond 2, the differences in maximum lift-drag ratio between the fully tapered plan forms tested appear to be small and hence the selection of a wing plan form for optimum range will probably depend on factors such as the landing characteristics or control adaptability.

2. In the same Mach number range the triangular plan form appears to offer the lowest values of minimum drag and will therefore be of interest for aircraft operating at low lift coefficients.

3. In the Mach number range below 1.6 the arrow wing appears to offer the highest maximum lift-drag ratios, although a well-designed cambered triangular wing may approach the arrow wing in efficiency and at the same time yield somewhat lower minimum drag values. In particular, the difference in maximum lift-drag ratio will depend on the amount of leading-edge thrust which can be realized in flight, whether the leading edge thrust is obtained on a rounded or a cambered leading edge.

Langley Aeronautical Laboratory,
National Advisory Committee for Aeronautics,
Langley Field, Va., May 25, 1951.

REFERENCES

1. Jones, Robert T.: Estimated Lift-Drag Ratios at Supersonic Speed. NACA TN 1350, 1947.

2. Puckett, A. E., and Stewart, H. J.: Aerodynamic Performance of Delta Wings at Supersonic Speeds. Jour. Aero. Sci., vol. 14, no. 10, Oct. 1947, pp. 567-578.

3. Madden, Robert T.: Aerodynamic Study of a Wing-Fuselage Combination Employing a Wing Swept Back 63° - Characteristics at a Mach Number of 1.53 Including Effect of Small Variations of Sweep. NACA RM A8J04, 1949.

4. Madden, Robert T.: Aerodynamic Study of a Wing-Fuselage Combination Employing a Wing Swept Back 63° - Investigation at a Mach Number of 1.53 To Determine the Effects of Cambering and Twisting the Wing for Uniform Load at a Lift Coefficient of 0.25. NACA RM A9C07, 1949.

5. Brown, Clinton E.: Theoretical Lift and Drag of Thin Triangular Wings at Supersonic Speeds. NACA Rep. 839, 1946. (Supersedes NACA TN 1183.)

6. Stewart, H. J.: The Lift of a Delta Wing at Supersonic Speeds. Quarterly Appl. Math., vol. IV, no. 3, Oct. 1946, pp. 246-254.

7. Harmon, Sidney M., and Jeffreys, Isabella: Theoretical Lift and Damping in Roll of Thin Wings With Arbitrary Sweep and Taper at Supersonic Speeds - Supersonic Leading and Trailing Edges. NACA TN 2114, 1950.

8. Puckett, Allen E.: Supersonic Wave Drag of Thin Airfoils. Jour. Aero. Sci., vol. 13, no. 9, Sept. 1946, pp. 475-484.

9. Nielsen, Jack N.: Effect of Aspect Ratio and Taper on the Pressure Drag at Supersonic Speeds of Unswept Wings at Zero Lift. NACA TN 1487, 1947.

10. Margolis, Kenneth: Supersonic Wave Drag of Sweptback Tapered Wings at Zero Lift. NACA TN 1448, 1947.

11. Love, Eugene S.: Investigations at Supersonic Speeds of 22 Triangular Wings Representing Two Airfoil Sections for Each of 11 Apex Angles. NACA Rep. 1238, 1955. (Supersedes NACA RM L9D07.)

12. Haack, W.: Geschossformen kleinsten Wellenwiderstandes. Bericht 139 der Lilienthal-Gesellschaft für Luftfahrtforschung, 1941, pp. 14-28.

13. Von Kármán, Theodor, and Moore, Norton B.: Resistance of Slender Bodies Moving With Supersonic Velocities With Special Reference to Projectiles. Trans. A.S.M.E., vol. 54, no. 23, Dec. 15, 1932, pp. 303-310.

14. Lighthill, M. J.: Supersonic Flow Past Bodies of Revolution. R. & M. No. 2003, British A.R.C., 1945.

15. Love, Eugene S.: Aerodynamic Investigation of a Parabolic Body of Revolution at Mach Number of 1.92 and Some Effects of an Annular Jet Exhausting From the Base. NACA TN 3709, 1956. (Supersedes NACA RM L9K09.)

16. Allen, H. Julian: Estimation of the Forces and Moments Acting on Inclined Bodies of Revolution of High Fineness Ratio. NACA RM A9I26, 1949.

17. Heitmeyer, John C.: Aerodynamic Study of a Wing-Fuselage Combination Employing a Wing Swept Back 63° - Effect of Reynolds Number at Supersonic Mach Numbers on the Longitudinal Characteristics of a Wing Twisted and Cambered for Uniform Load. NACA RM A50G10, 1950.

18. Olson, Robert N., and Mead, Merrill H.: Aerodynamic Study of a Wing-Fuselage Combination Employing a Wing Swept Back 63° - Effectiveness at Supersonic Speeds of a 30-Percent Chord, 50-Percent Semispan Elevon as a Lateral Control Device. NACA RM A50K07, 1951.

19. Lindsey, W. F., Daley, Bernard N., and Humphreys, Milton D.: The Flow and Force Characteristics of Supersonic Airfoils at High Subsonic Speeds. NACA TN 1211, 1947.

TABLE I.- SUMMARY OF GEOMETRIC PROPERTIES OF WINGS

[The aspect ratios and mean geometric chords are based on the wing area including that blanketed by the fuselage]

Plan form	Λ_{LE} (deg)	Λ_{TE} (deg)	A	S (sq in.)	b (in.)	$\bar{c}$ (in.)	t/c, percent, at -		k	j
							Root	0.75 b/2		
Diamond	38.6	38.6	2.50	13.35	5.78	3.08	1.40	2.15	50.0	58.2
Diamond	29.6	29.6	3.50	13.00	6.76	2.56	2.00	3.07	50.0	58.2
Triangular	68.6	0	1.57	14.10	4.70	4.00	2.00	3.07	30.0	73.4
Arrow	68.6	45.0	2.57	8.58	4.70	2.43	3.29	5.06	49.3	73.4

TABLE II.- SUMMARY OF AERODYNAMIC CHARACTERISTICS OF VARIOUS CONFIGURATIONS.

[The values of C_{L_α} are average values taken over the range of $C_L = 0$ to $C_L = 0.15$; the Reynolds numbers are based on the mean aerodynamic chord of the wing]

Configuration	Incidence	M	$(L/D)_{max}$	$C_{D_{min}}$	C_{L_α}	$C_{L_{opt}}$	R
A = 2.5 flat diamond wing on body	0°	1.62	8.11	0.0097	0.0475	0.154	1.111×10^6
		1.93	7.60	.0086	.0389	.140	.998
		2.41	6.79	.0084	.0306	.116	.798
	3°	1.62	8.05	.0101	.0483	.160	1.111
A = 3.5 flat diamond wing on body	0°	1.62	7.66	.0119	.0509	.178	.924
		1.93	7.11	.0107	.0402	.154	.830
		2.41	6.51	.0097	.0313	.143	.663
Flat triangular wing on body	0°	1.62	7.35	.0088	.0352	.146	1.445
		1.93	7.10	.0076	.0306	.126	1.295
		2.41	6.70	.0072	.0249	.107	1.036
	3°	1.62	7.19	.0087	.0353	.145	1.445
$C_{L_{Des}}$ = 0.08 triangular wing on body	0°	1.62	8.12	.0092	.0343	.122	1.445
		1.93	7.76	.0080	.0300	.116	1.295
		2.41	6.81	.0084	.0248	.104	1.036
	3°	2.41	6.69	.0084	.0246	.107	1.036
$C_{L_{Des}}$ = 0.20 triangular wing on body	0°	1.62	8.05	.0124	.0356	.156	1.445
		1.93	7.63	.0112	.0320	.138	1.295
		2.41	6.72	.0110	.0254	.116	1.036
	3°	1.62	8.01	.0125	.0349	.148	1.445
		1.93	7.34	.0114	.0306	.138	1.295
Flat arrow wing on body	0°	1.62	6.77	.0112	.0375	.161	.878
		1.93	6.46	.0103	.0335	.147	.788
		2.41	6.04	.0102	.0274	.118	.630
$C_{L_{Des}}$ = 0.08 arrow wing on body	0°	1.62	7.86	.0119	.0373	.161	.878
		1.93	7.20	.0111	.0320	.149	.788
$C_{L_{Des}}$ = 0.20 arrow wing on body	0°	1.62	7.91	.0157	.0378	.192	.878
		1.93	7.28	.0136	.0330	.183	.788
		2.41	6.32	.0131	.0270	.138	.630

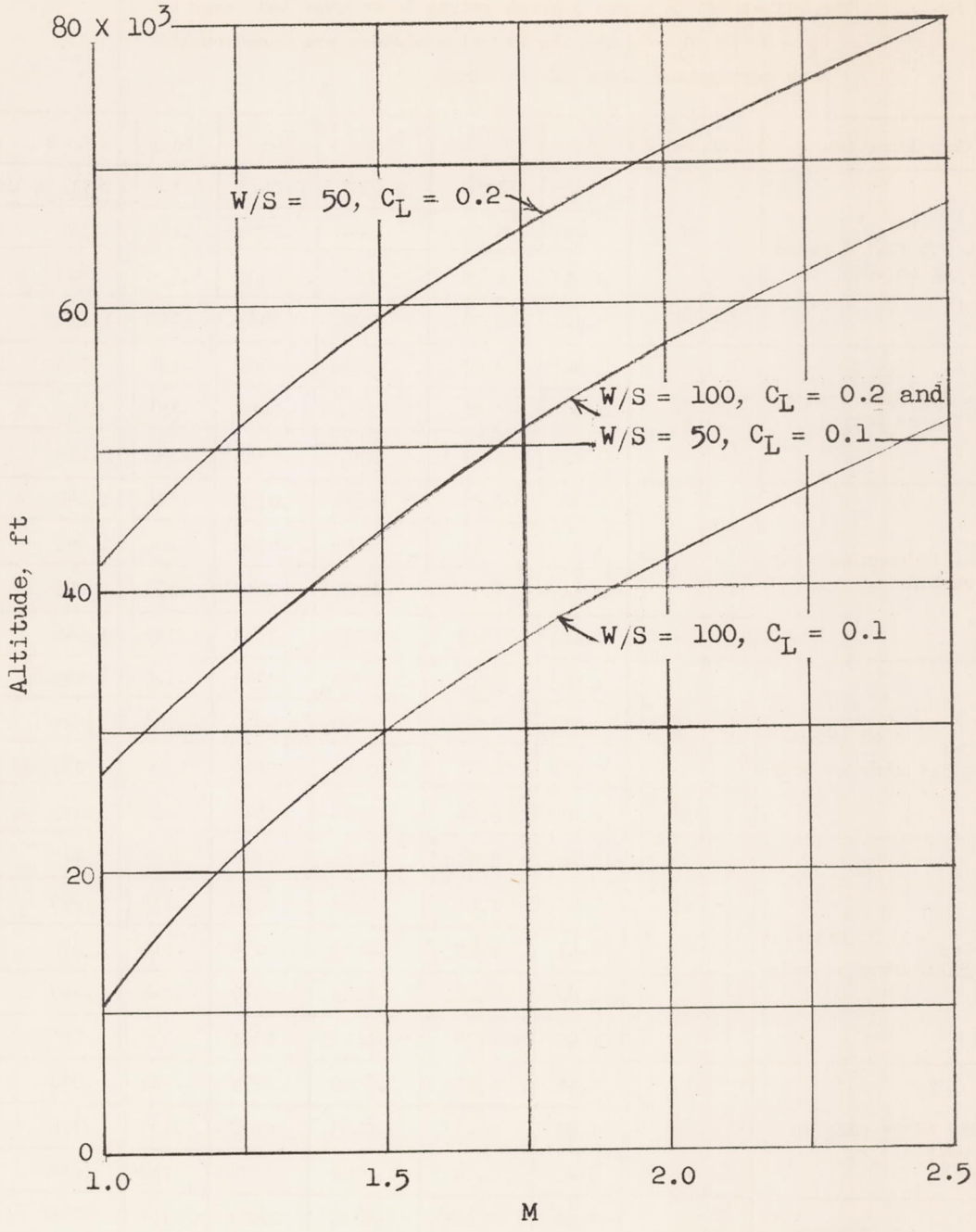

Figure 1.- Variation of altitude with Mach number for level flight at various values of wing loading and lift coefficient.

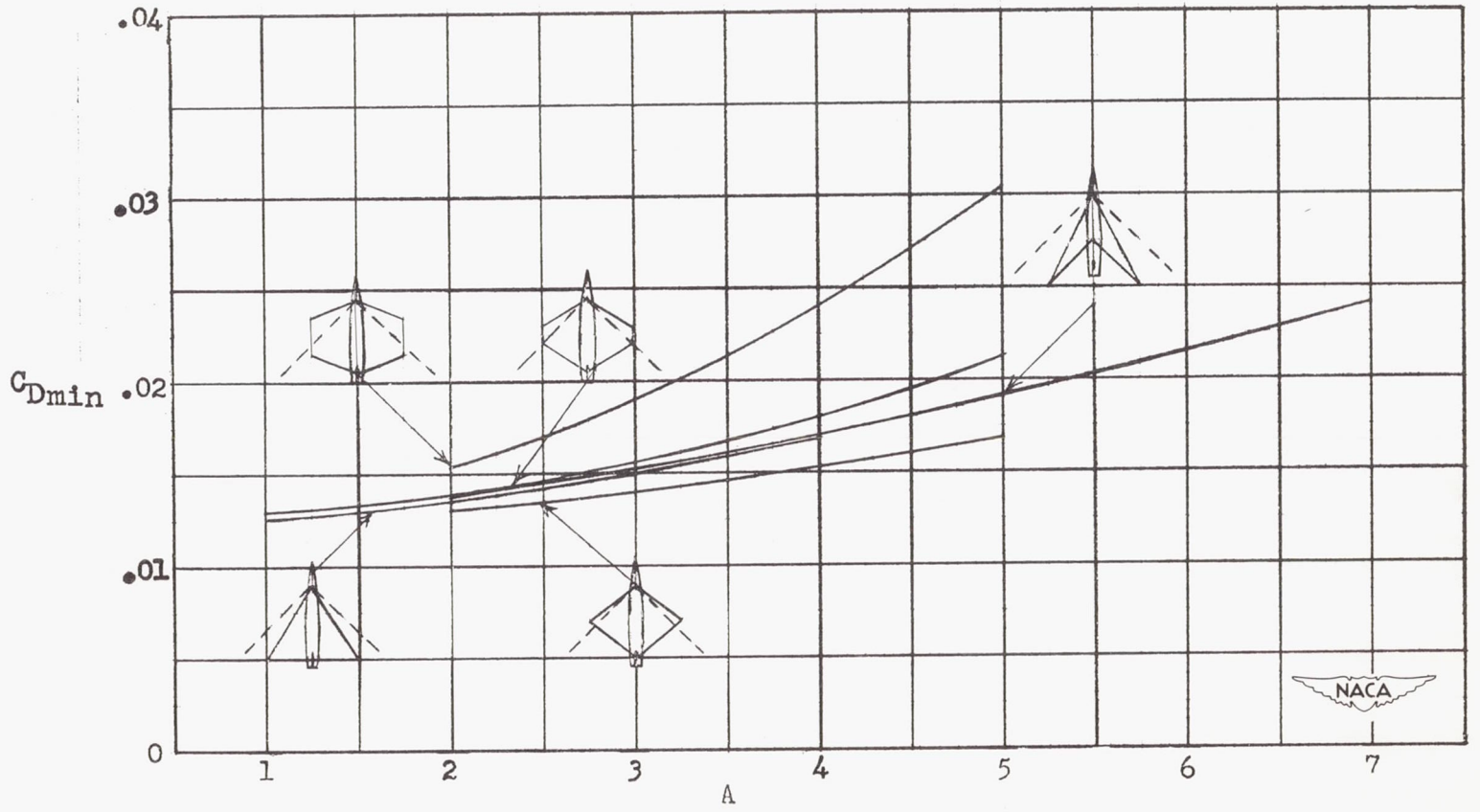

Figure 2.- Theoretical variation of $C_{D_{min}}$ with aspect ratio for various wing-tail-fuselage combinations at M = 1.41.

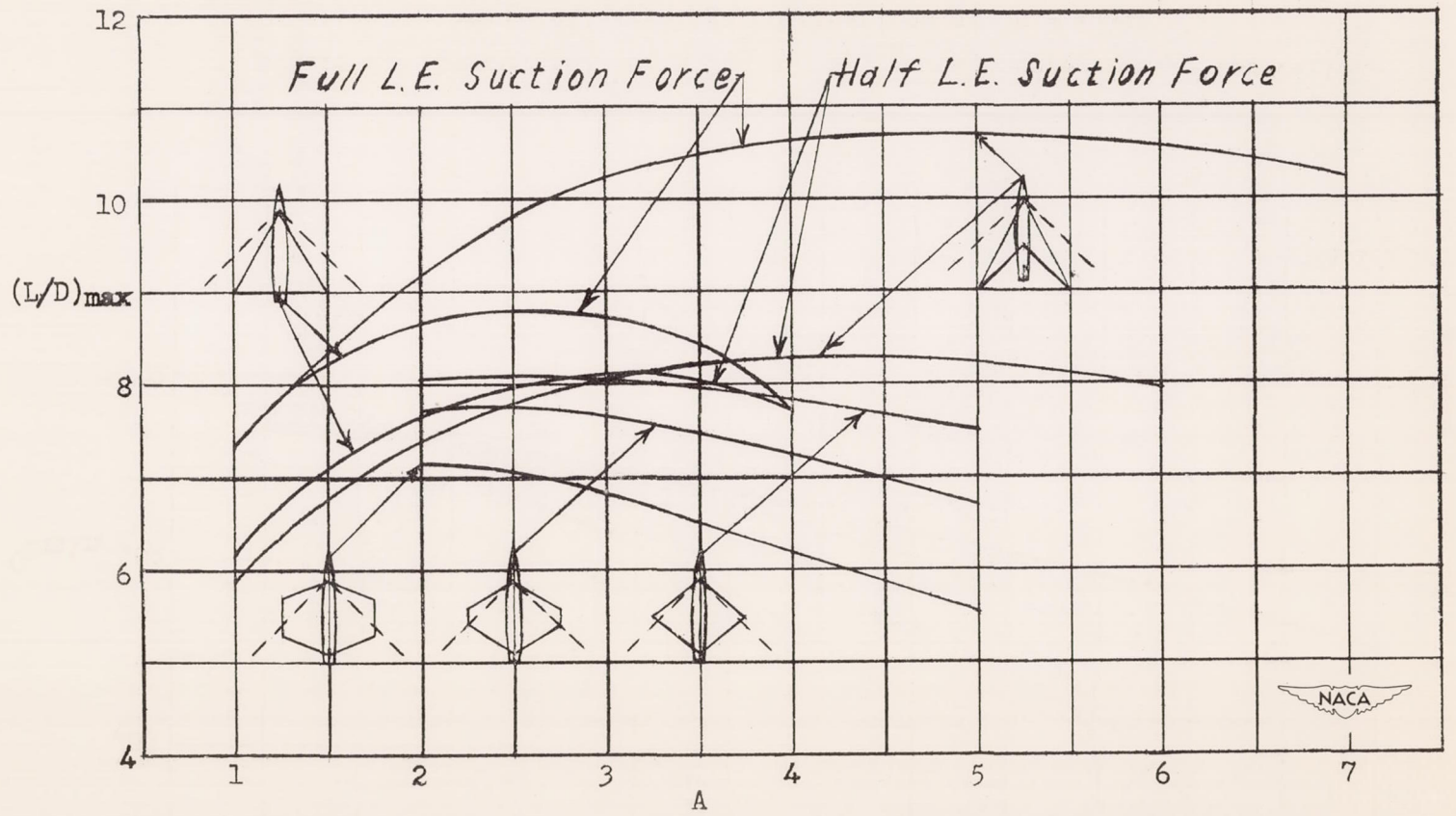

Figure 3.- Theoretical variation of $(L/D)_{max}$ with aspect ratio for various wing-tail-fuselage combinations at $M = 1.41$.

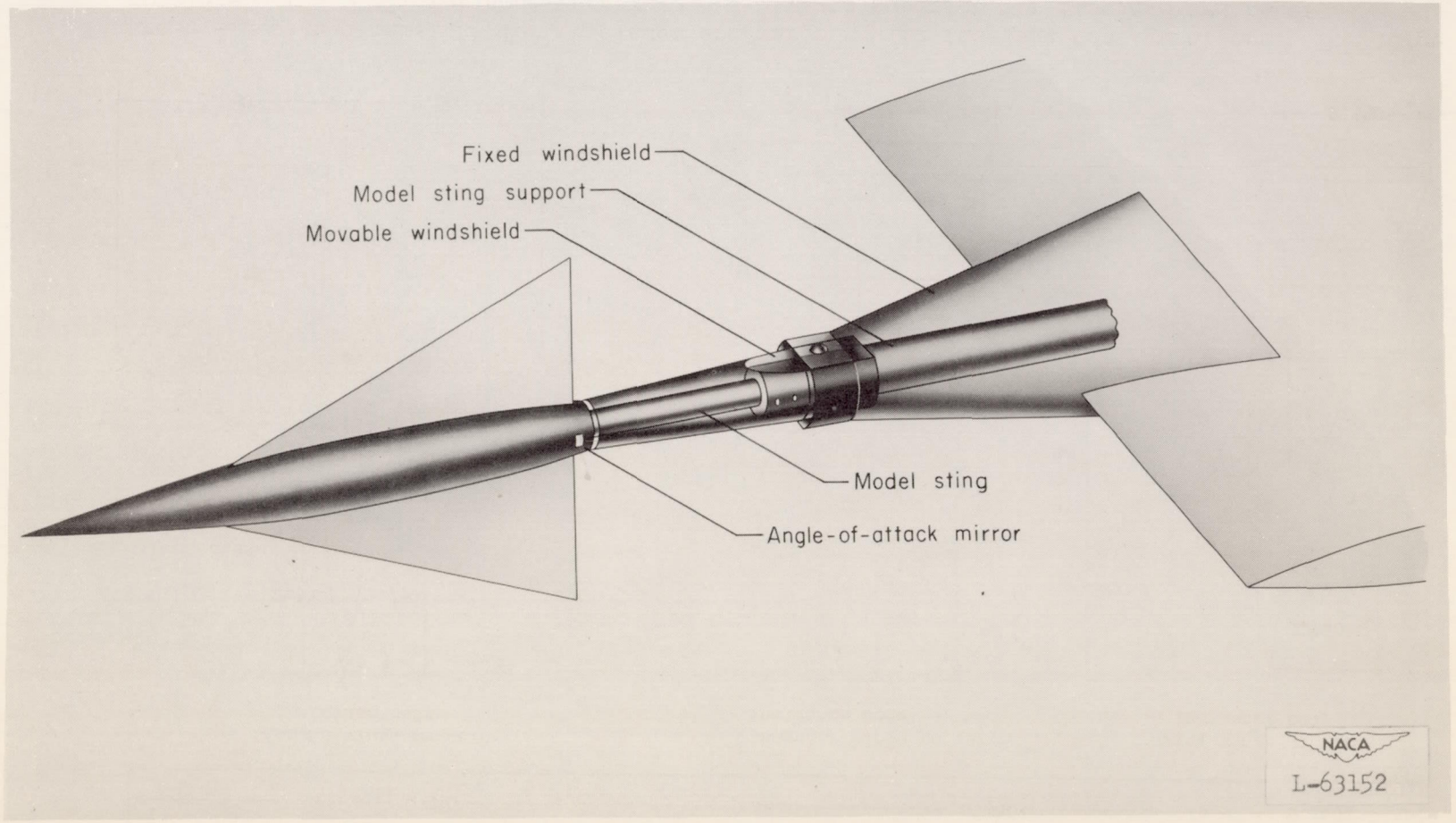

Figure 4.- Model support system.

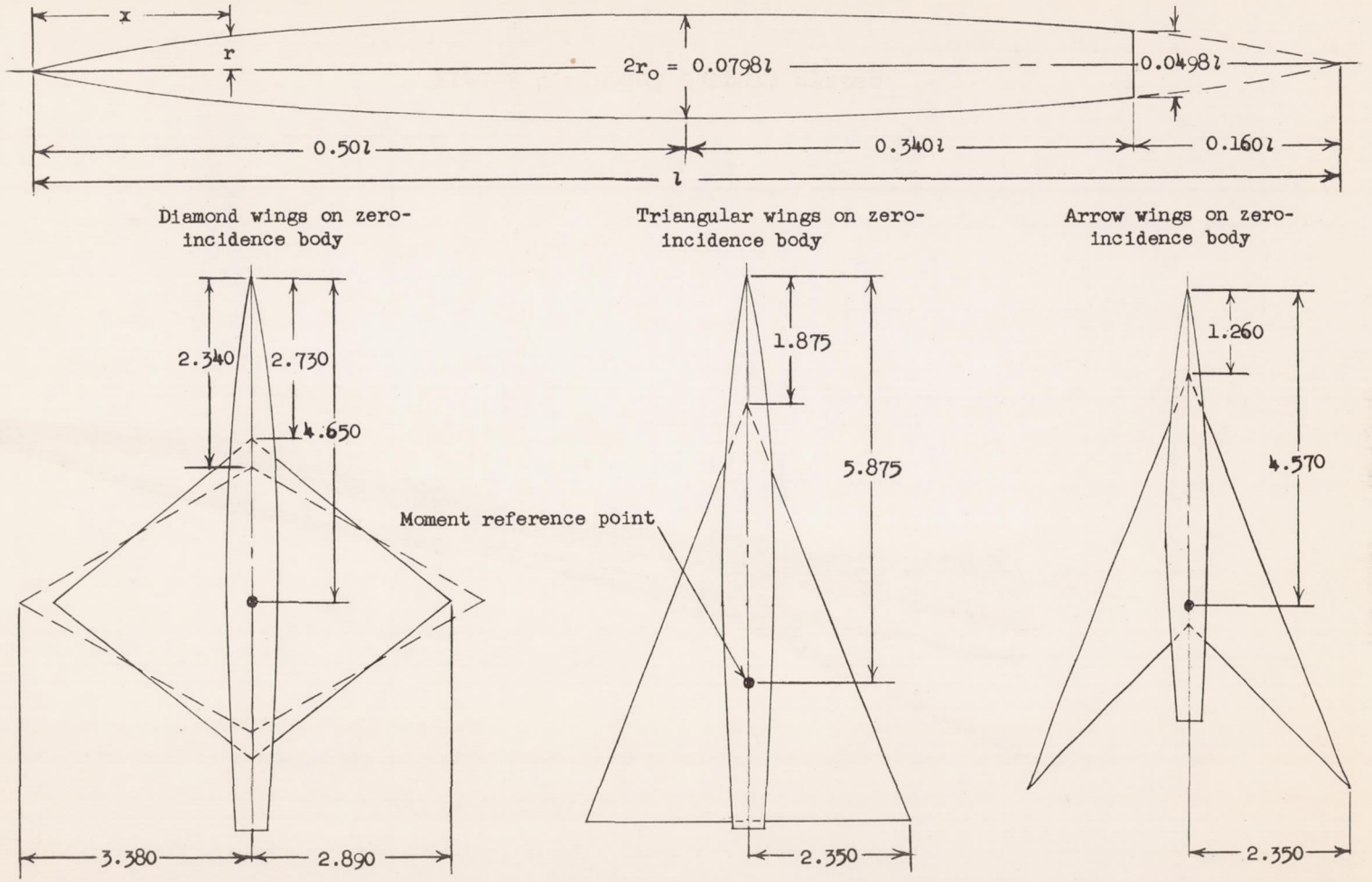

Figure 5.- Design dimensions for fuselages and various wing-fuselage configurations. For large fuselage, $\ell = 9.52$; for small fuselage, $\ell = 7.41$; equation for fuselage ordinates, $\frac{r}{r_o} = \left[1 - \left(1 - \frac{2x}{\ell}\right)^2\right]^{3/4}$; fineness ratio $\frac{\ell}{2r_o} = 12.53$. All dimensions are in inches.

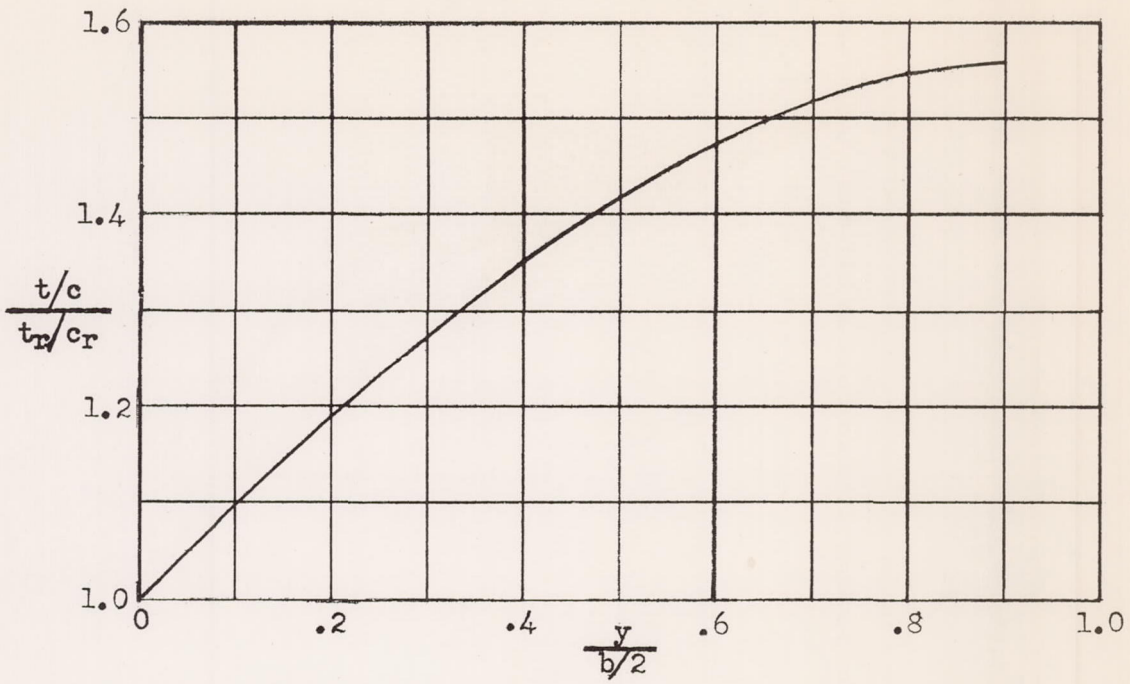

(a) Variation of the spanwise thickness ratio of all wings.

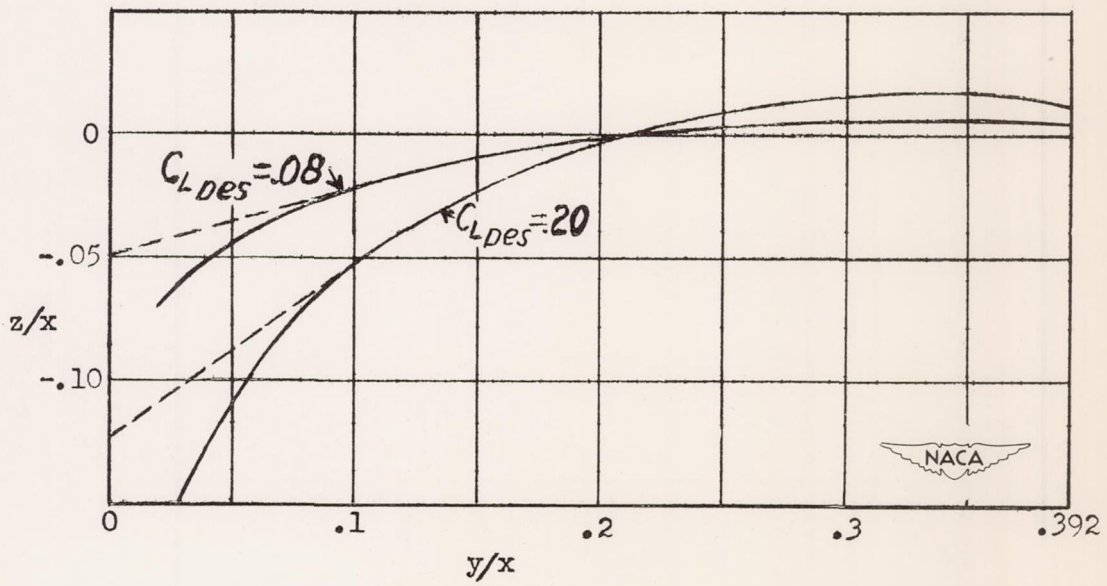

(b) Spanwise camber lines for the $C_{L_{Des}} = 0.08$ and $C_{L_{Des}} = 0.20$ cambered triangular wings.

Figure 6.- Airfoil properties of various wings.

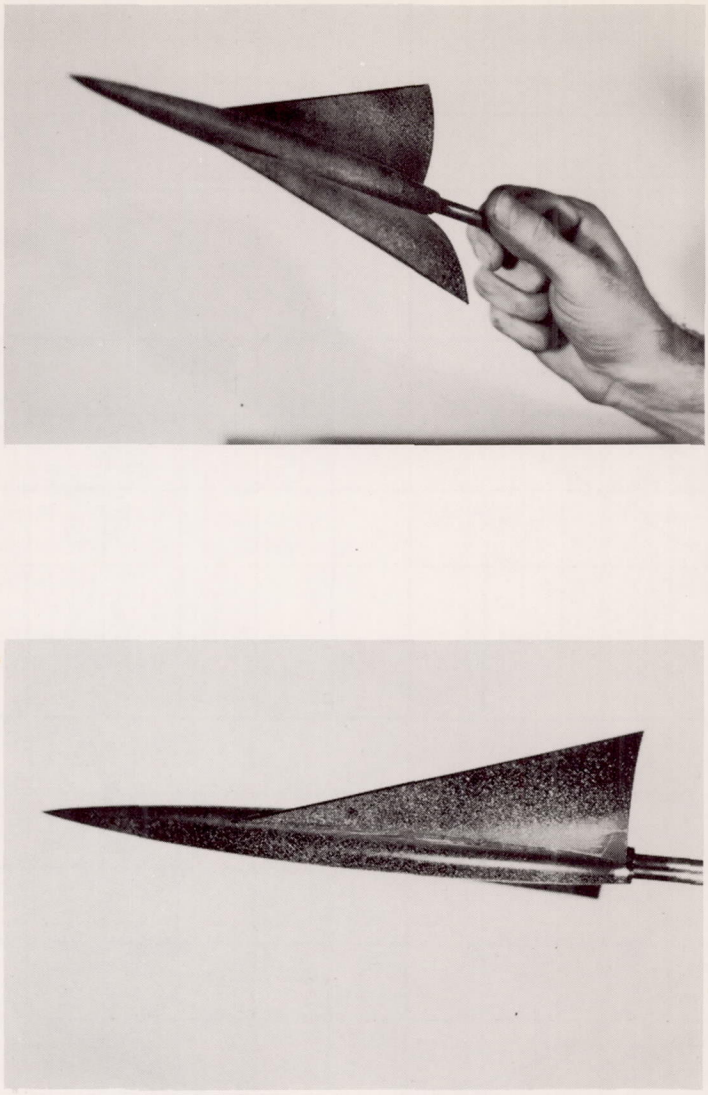

NACA
L-69133

Figure 7.- $C_{L_{Des}} = 0.20$ cambered triangular wing on body at 0° incidence.

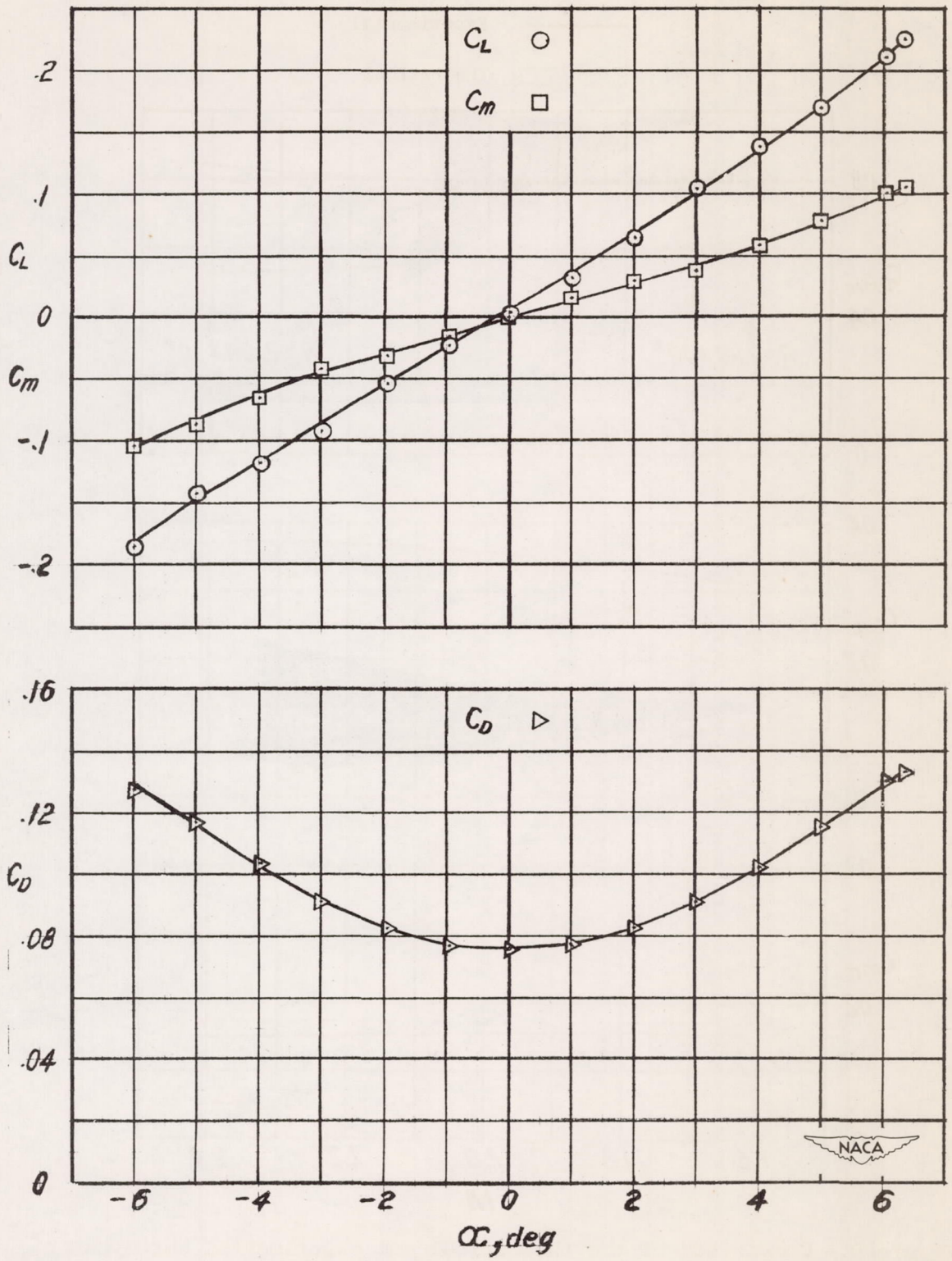

Figure 8.- Aerodynamic characteristics of the fuselage alone at M = 1.62 and R = 2.89 × 10^6. Reynolds number and coefficients based on fuselage length and frontal area. Moment taken about maximum-diameter position.

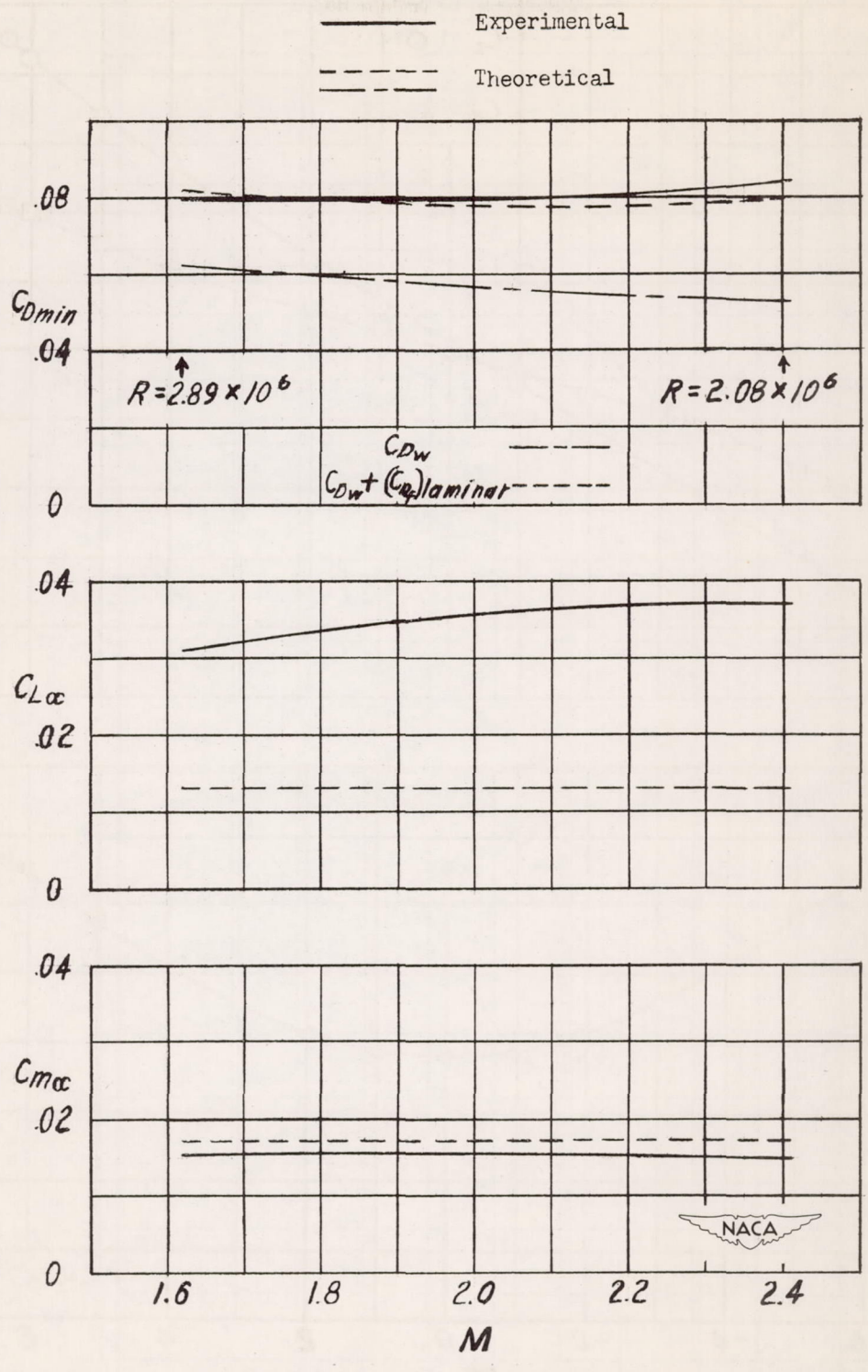

Figure 9.- Comparison of the theoretical and experimental aerodynamic characteristics of the fuselage alone. C_{L_α} and C_{m_α} are the slopes through zero lift and moment. Moment taken about maximum-diameter position.

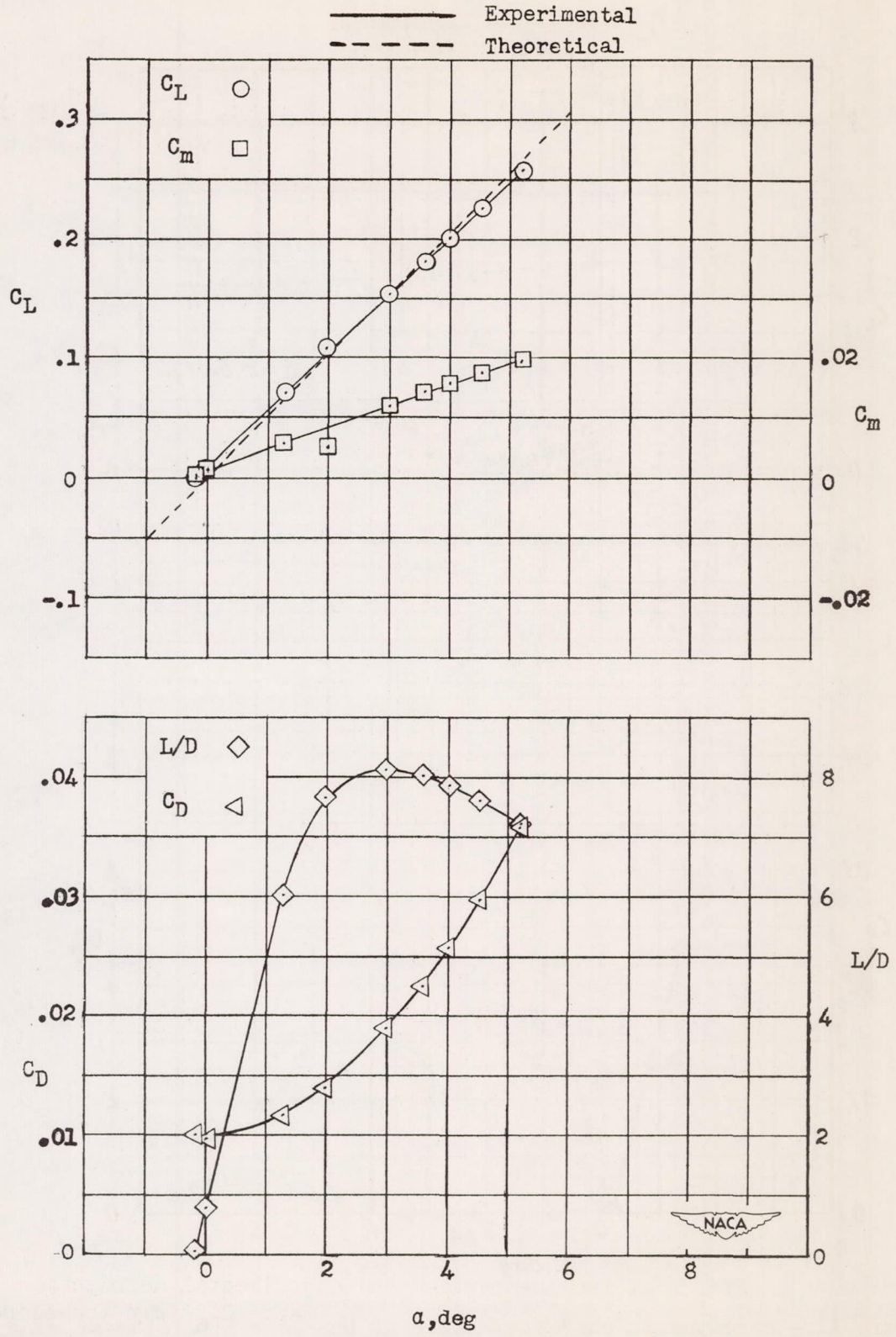

Figure 10.- Aerodynamic characteristics of the A = 2.5 diamond wing on body at 0° incidence at M = 1.62 and R = 1.11×10^6.

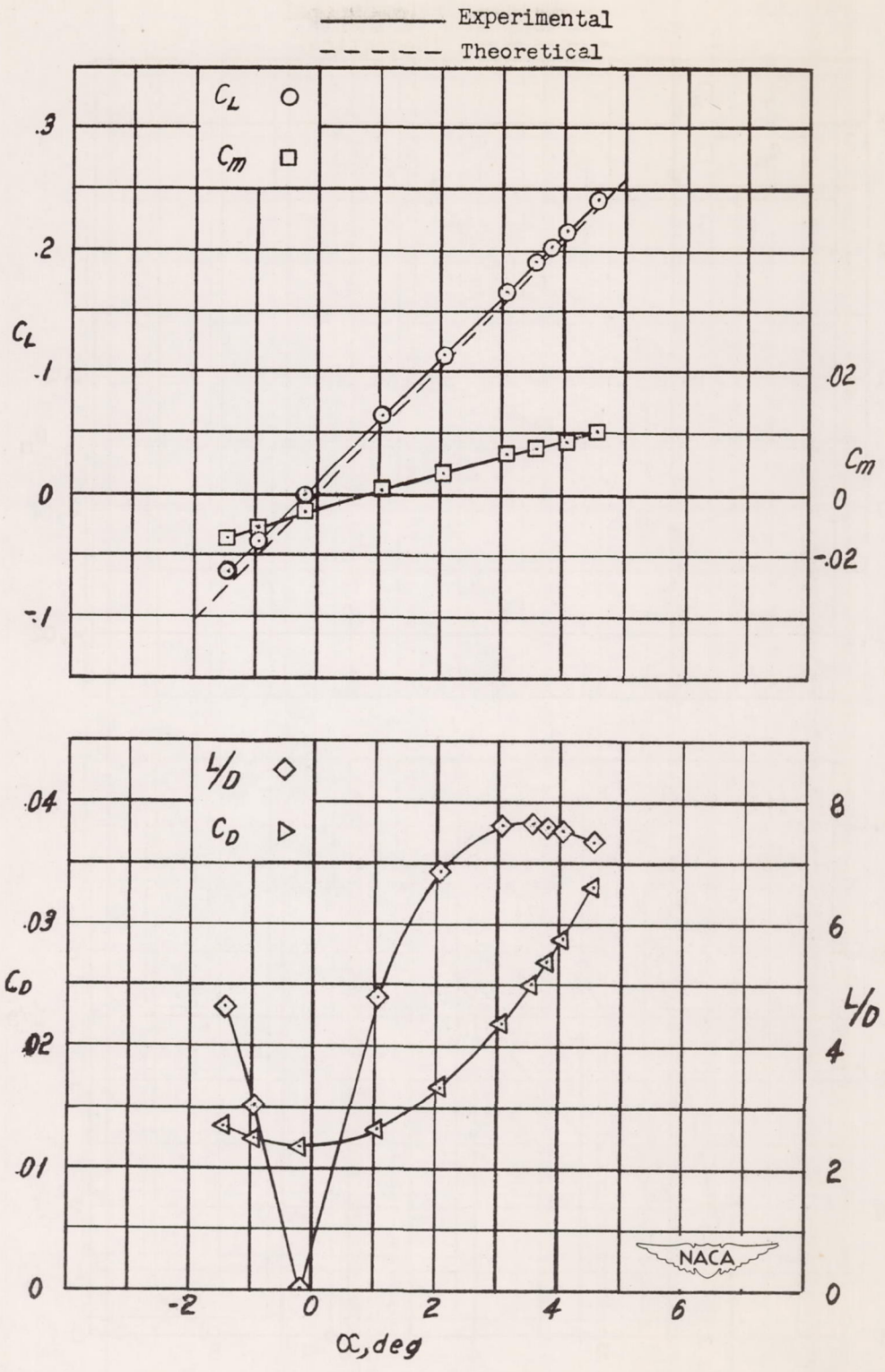

Figure 11.- Aerodynamic characteristics of the A = 3.5 diamond wing on body at 0° incidence at M = 1.62 and R = 0.92×10^6.

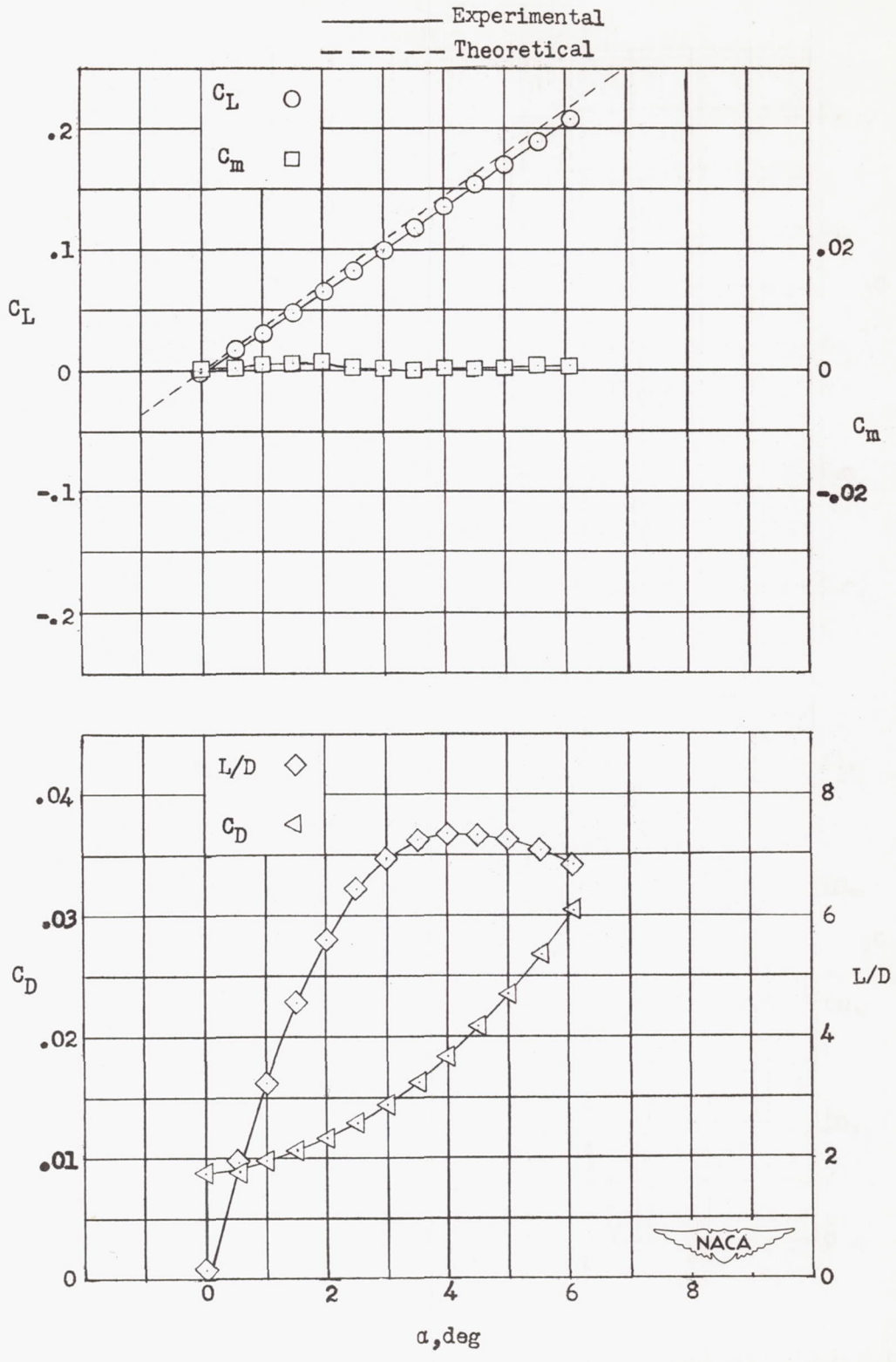

Figure 12.- Aerodynamic characteristics of the flat triangular wing on body at 0° incidence at $M = 1.62$ and $R = 1.45 \times 10^6$.

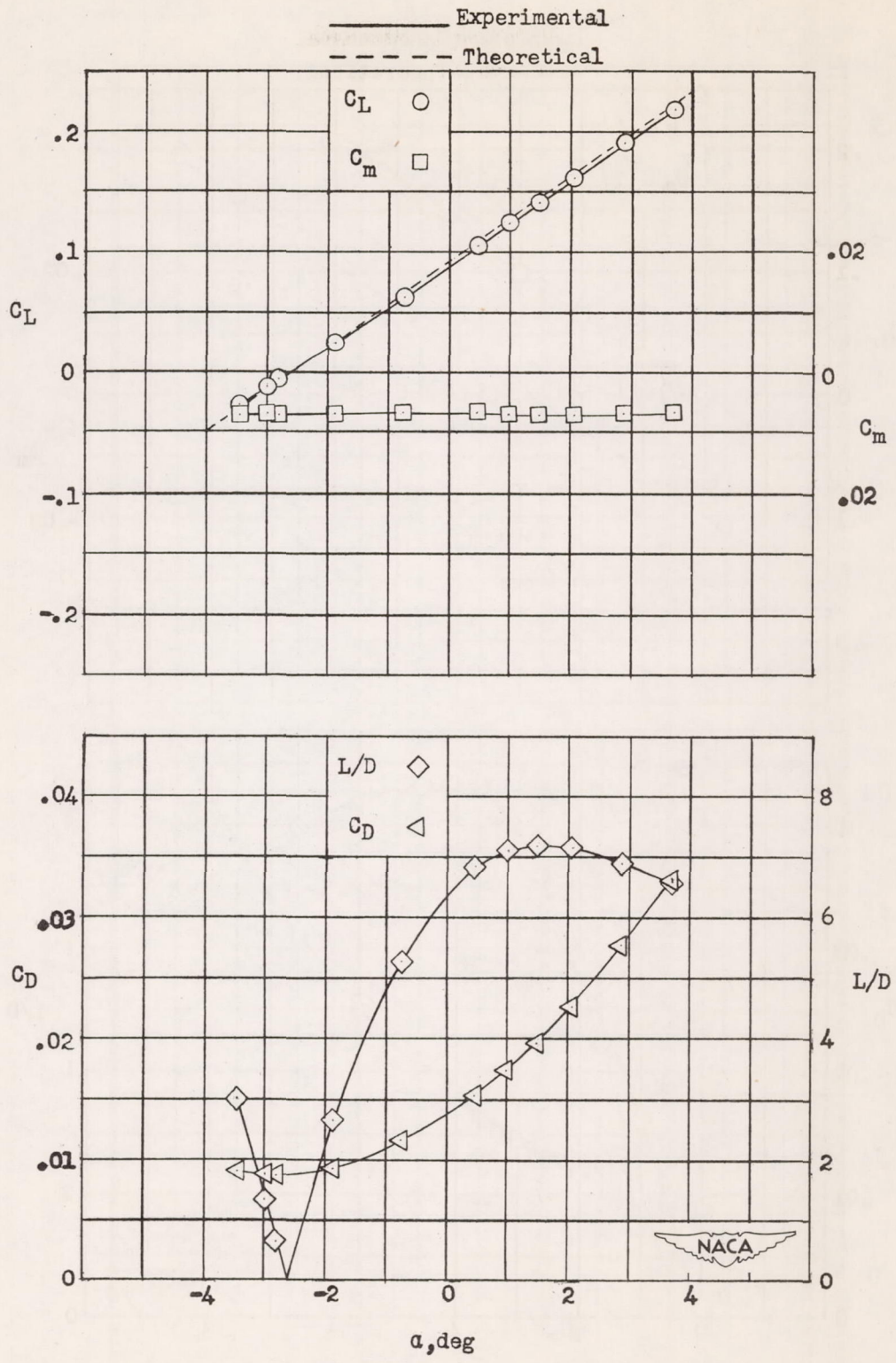

Figure 13.- Aerodynamic characteristics of the flat triangular wing on body at 3^{o} incidence at $M = 1.62$ and $R = 1.45 \times 10^{6}$.

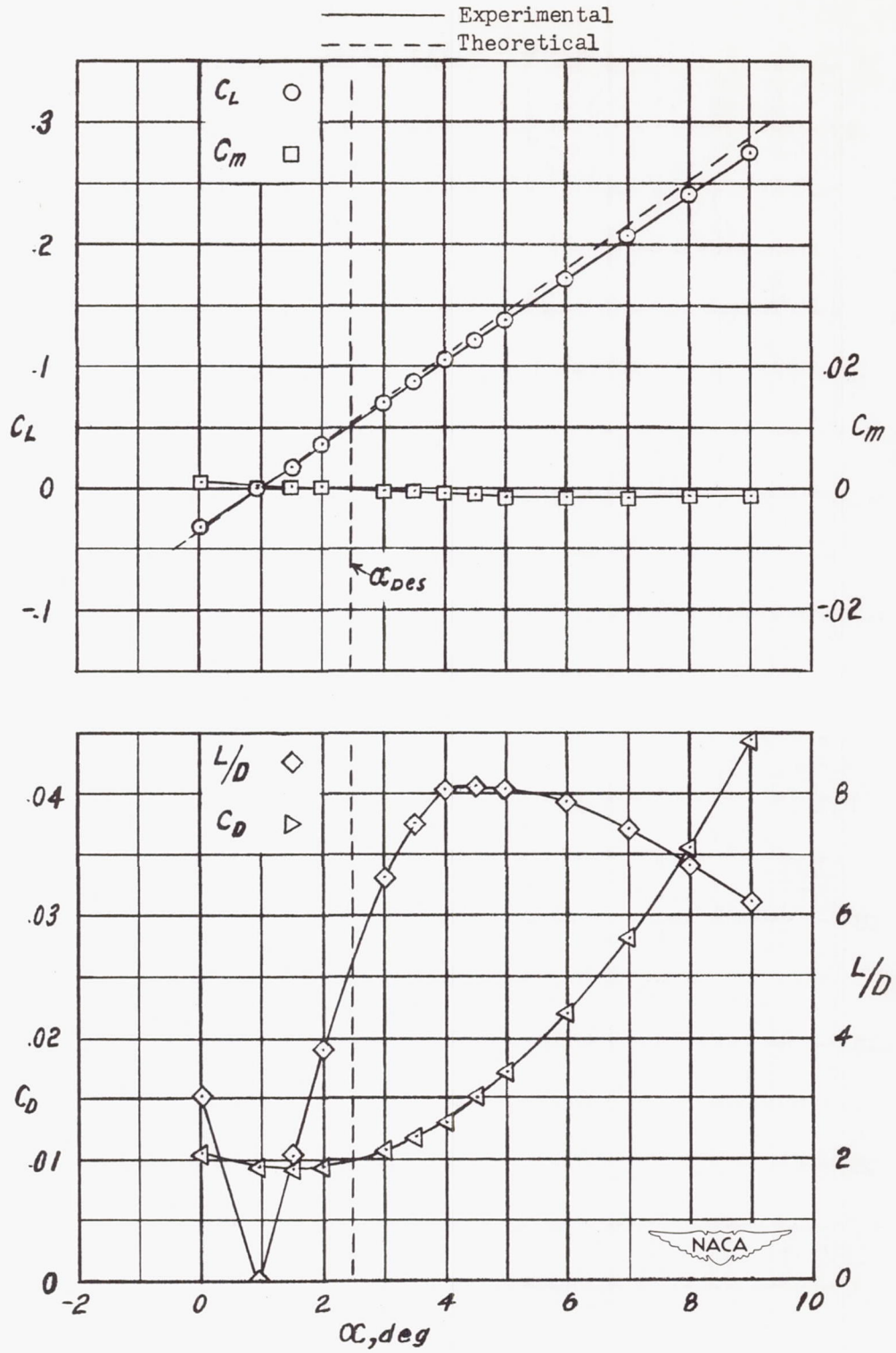

Figure 14.- Aerodynamic characteristics of the $C_{L_{Des}} = 0.08$ triangular wing on body at 0° incidence at $M = 1.62$ and $R = 1.45 \times 10^6$.

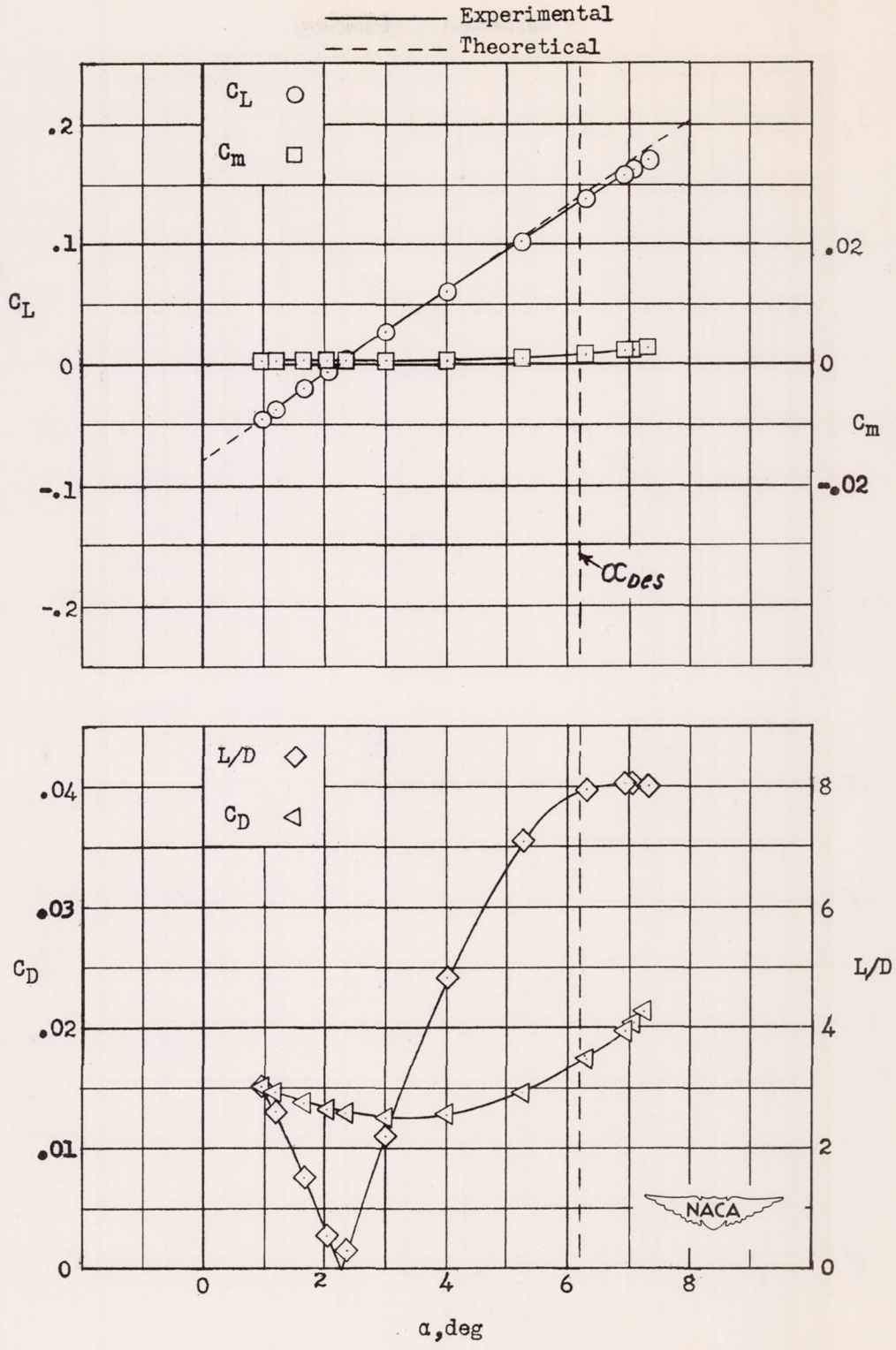

Figure 15.- Aerodynamic characteristics of the $C_{L_{Des}} = 0.20$ triangular wing on body at 0° incidence at $M = 1.62$ and $R = 1.45 \times 10^6$.

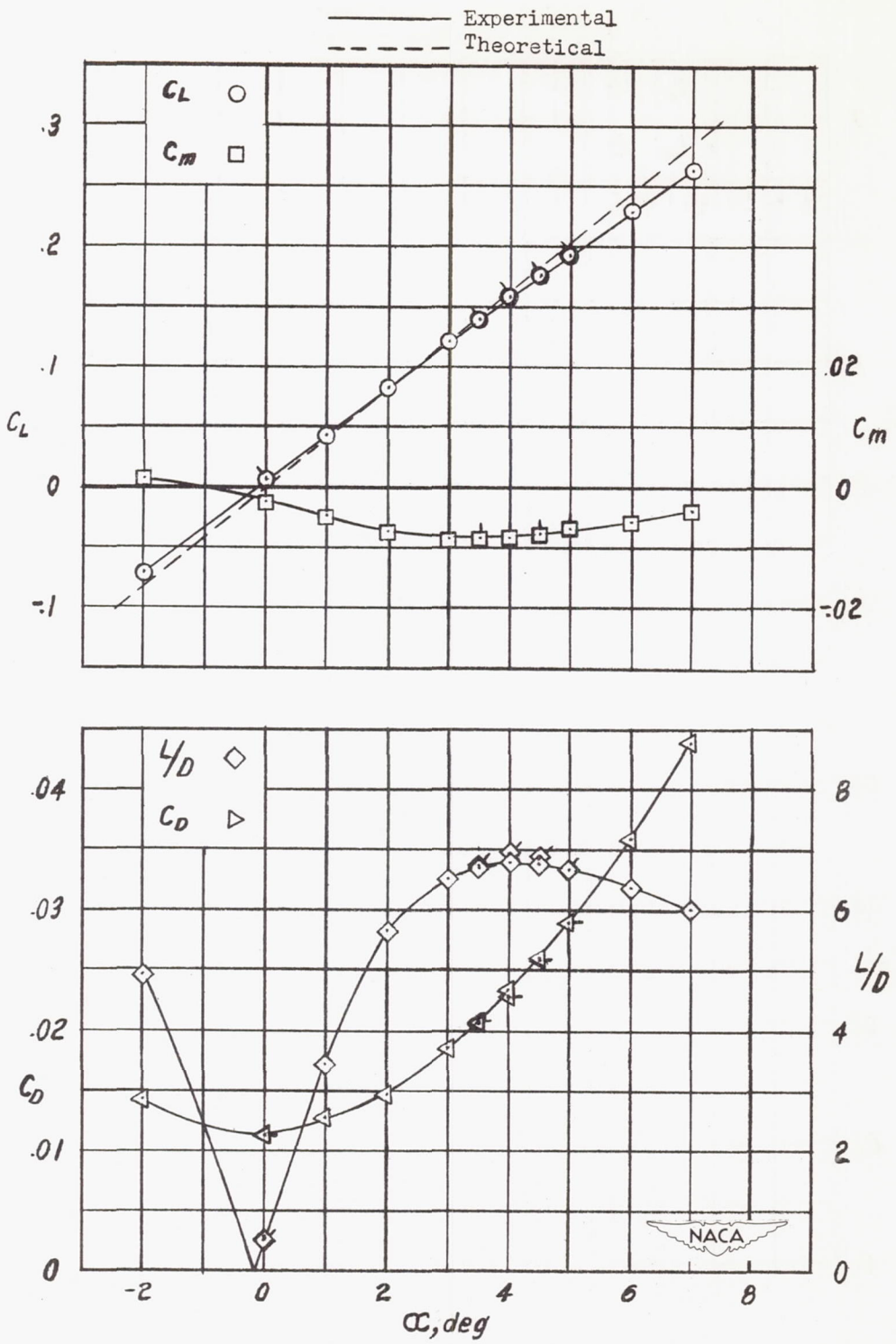

Figure 16.- Aerodynamic characteristics of the flat arrow wing on body at 0° incidence at $M = 1.62$ and $R = 0.88 \times 10^6$. Flagged points, $R = 1.13 \times 10^6$.

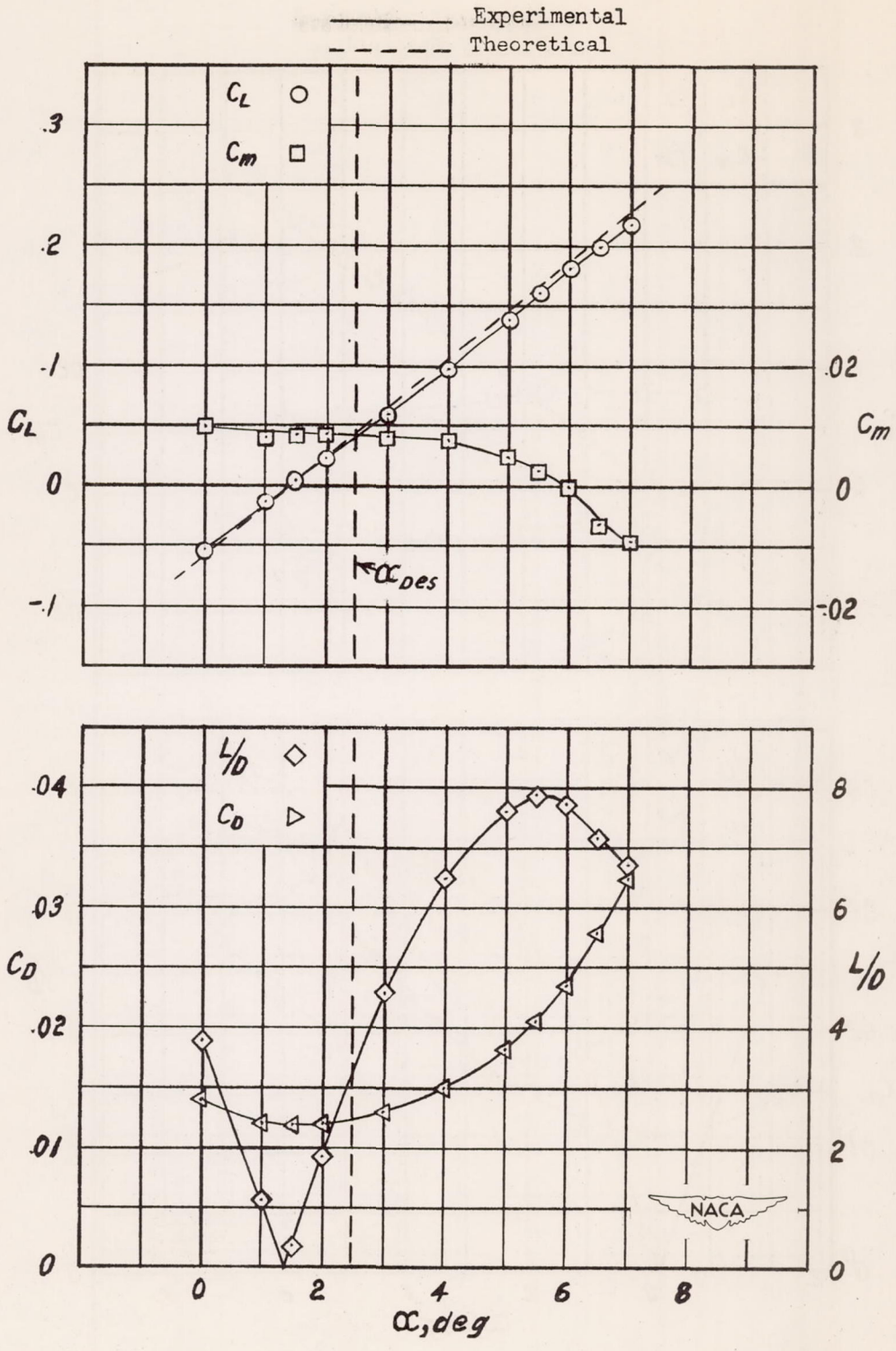

Figure 17.- Aerodynamic characteristics of the $C_{L_{Des}} = 0.08$ arrow wing on body at 0° incidence at $M = 1.62$ and $R = 0.88 \times 10^6$.

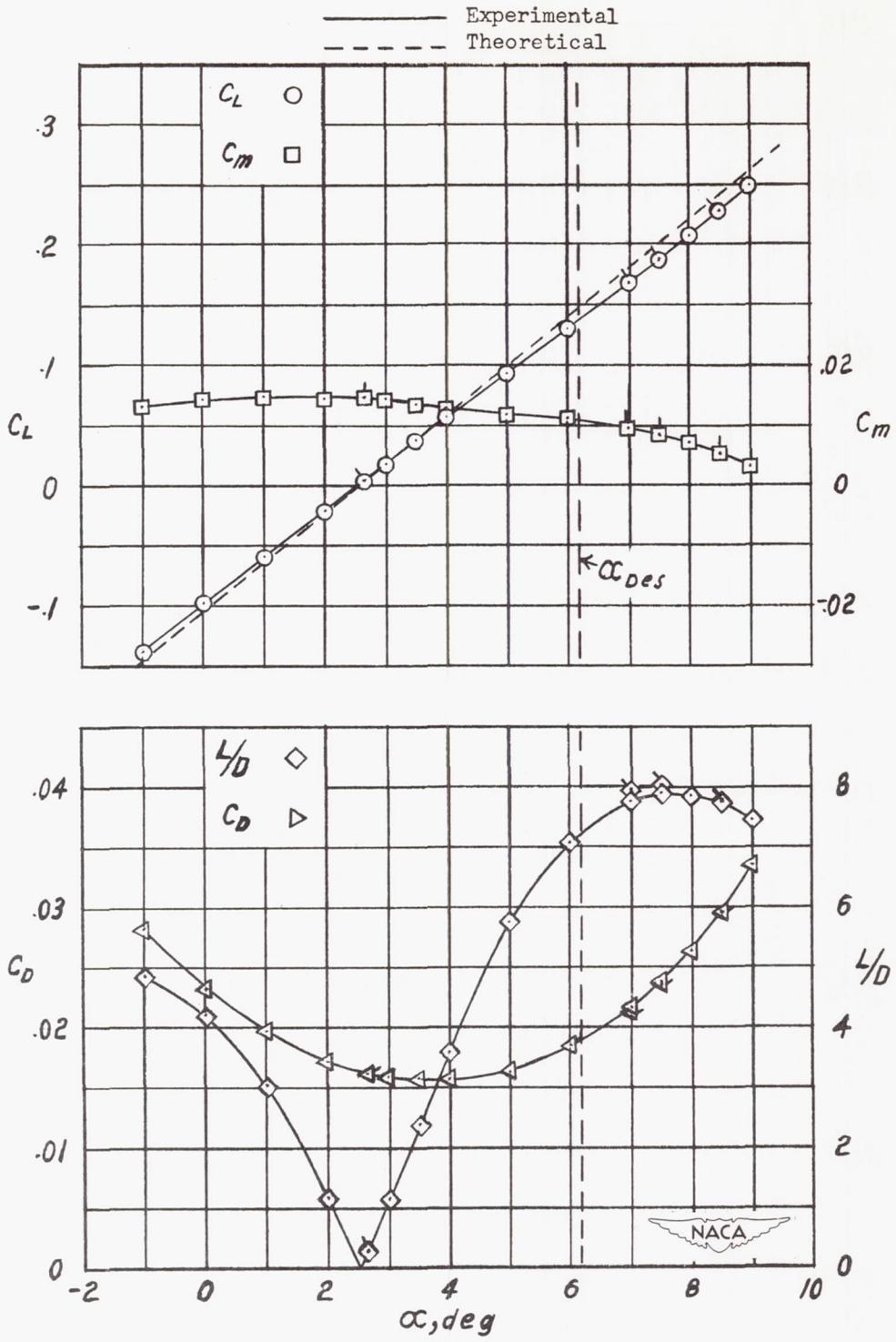

Figure 18.- Aerodynamic characteristics of the $C_{L_{Des}} = 0.20$ arrow wing on body at 0° incidence at $M = 1.62$ and $R = 0.88 \times 10^6$. Flagged points, $R = 1.13 \times 10^6$.

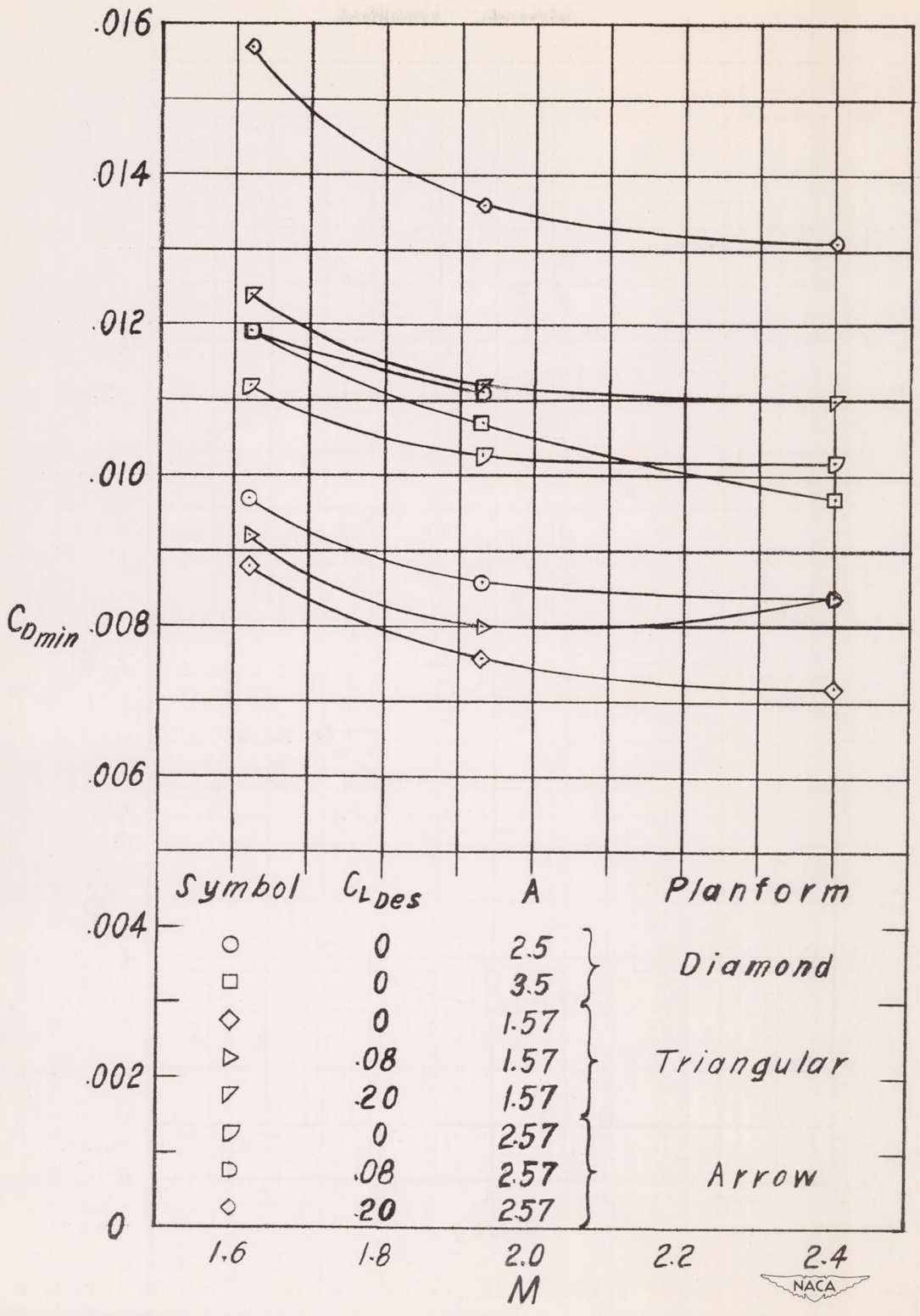

Figure 19.- Summary of experimental minimum drag coefficients of various configurations.

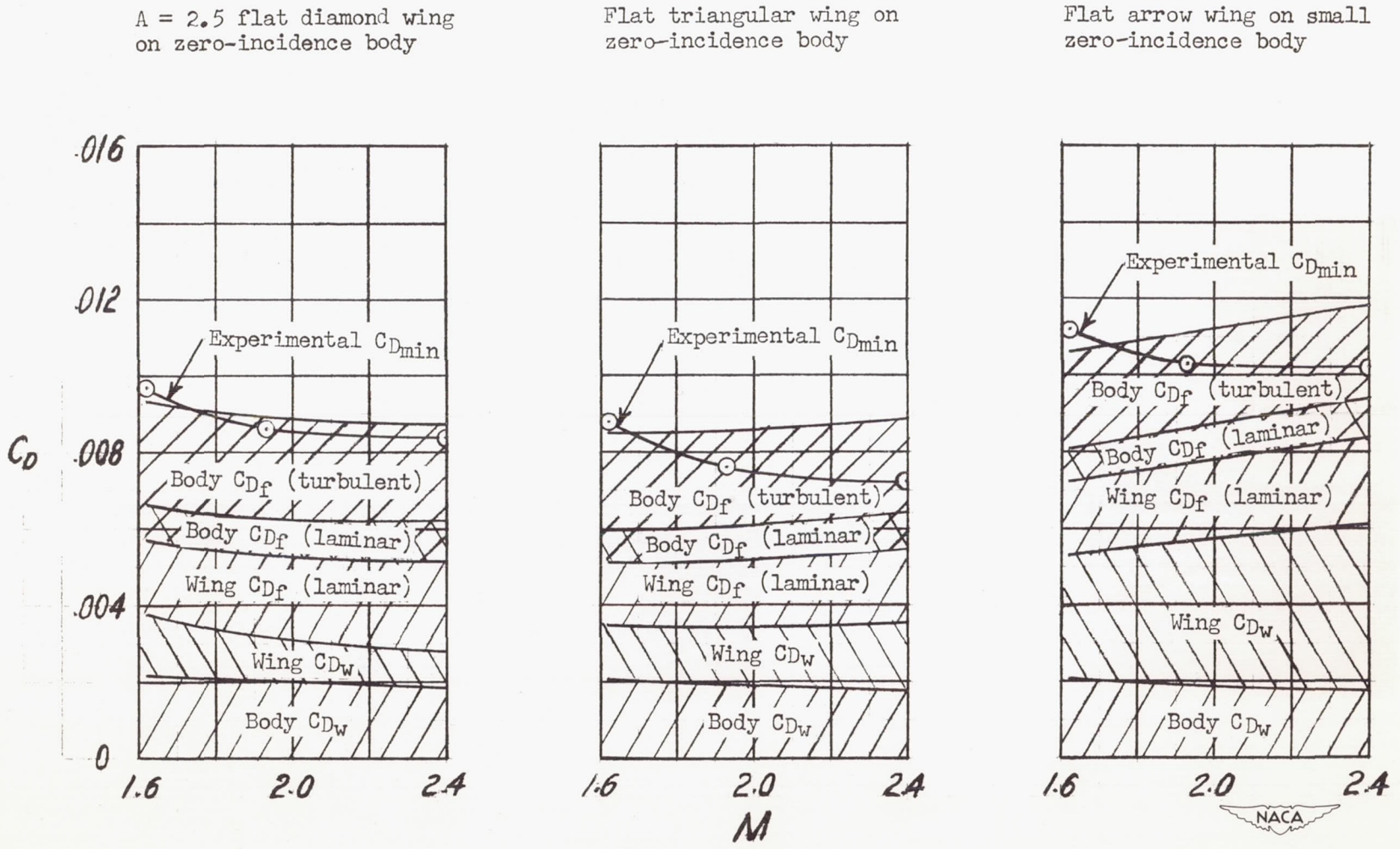

Figure 20.- Drag breakdown for various configurations.

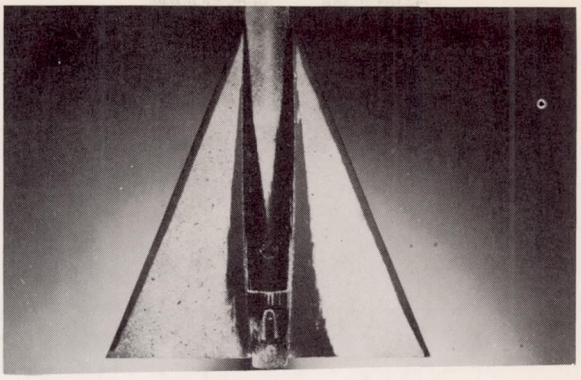

M = 1.62.

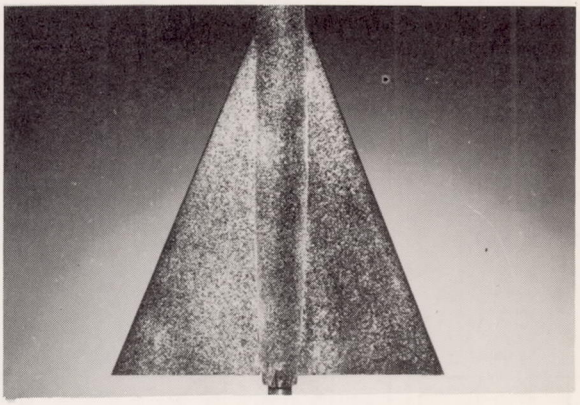

M = 2.40.

NACA
L-69134

Figure 21.- Liquid-film pictures of the flat triangular wing on the zero-incidence body at $\alpha = 0^{\circ}$.

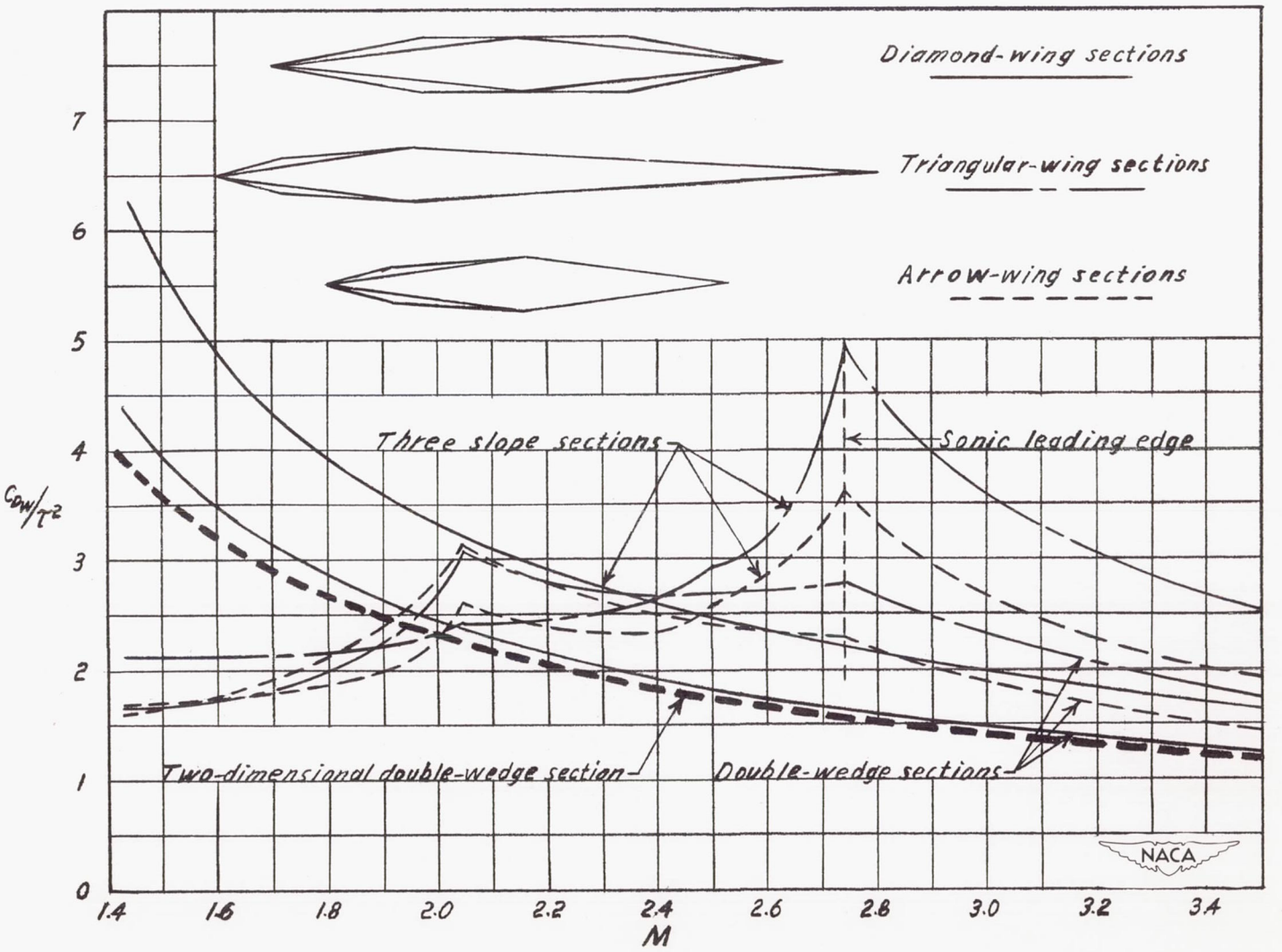

Figure 22.- Some effects of section shape on the theoretical wave drag of various wings.

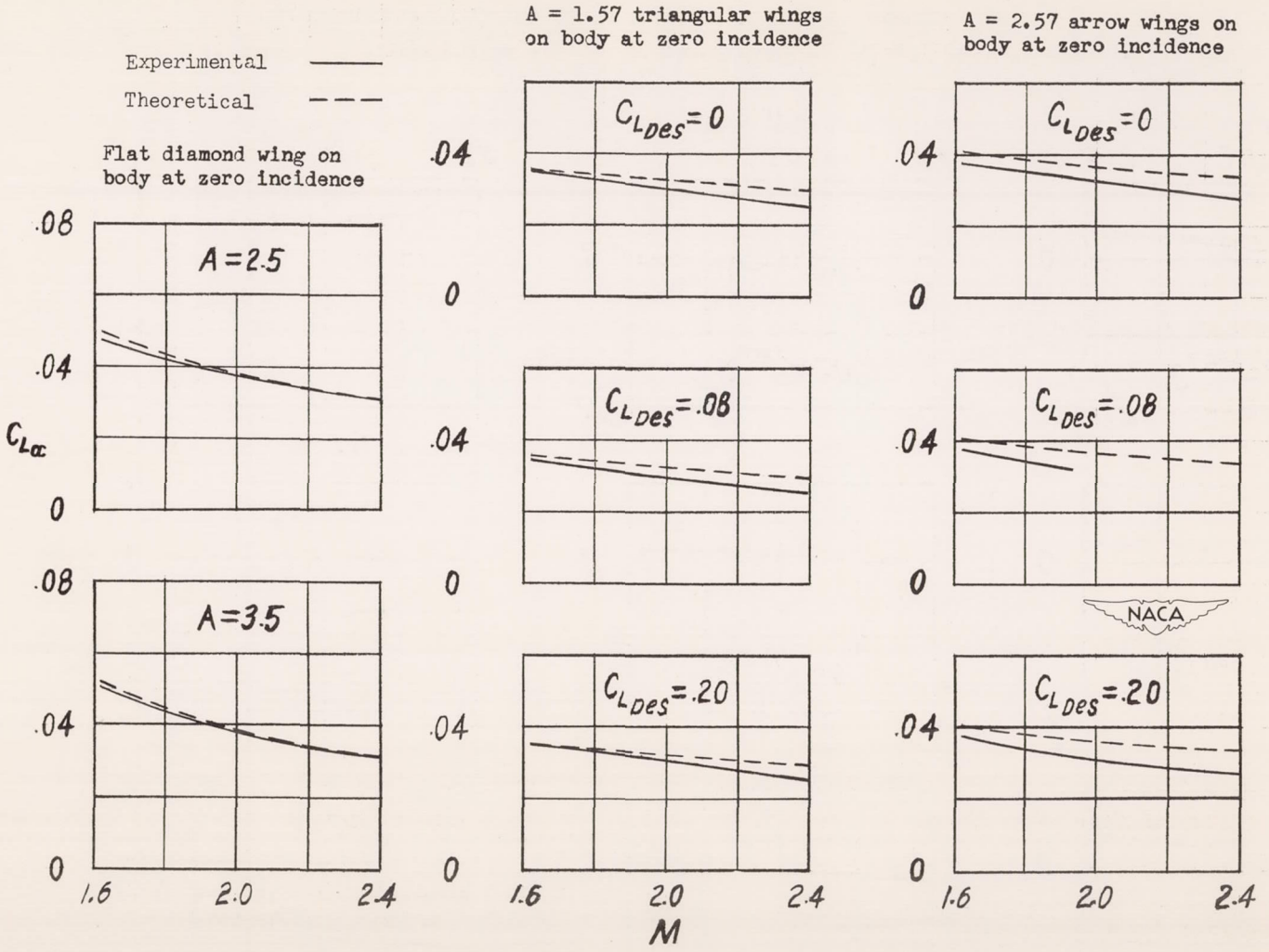

Figure 23.- Comparison of the experimental and theoretical lift-curve slopes of various configurations. The experimental lift-curve slope is an average value taken between lift coefficients of 0 and 0.15.

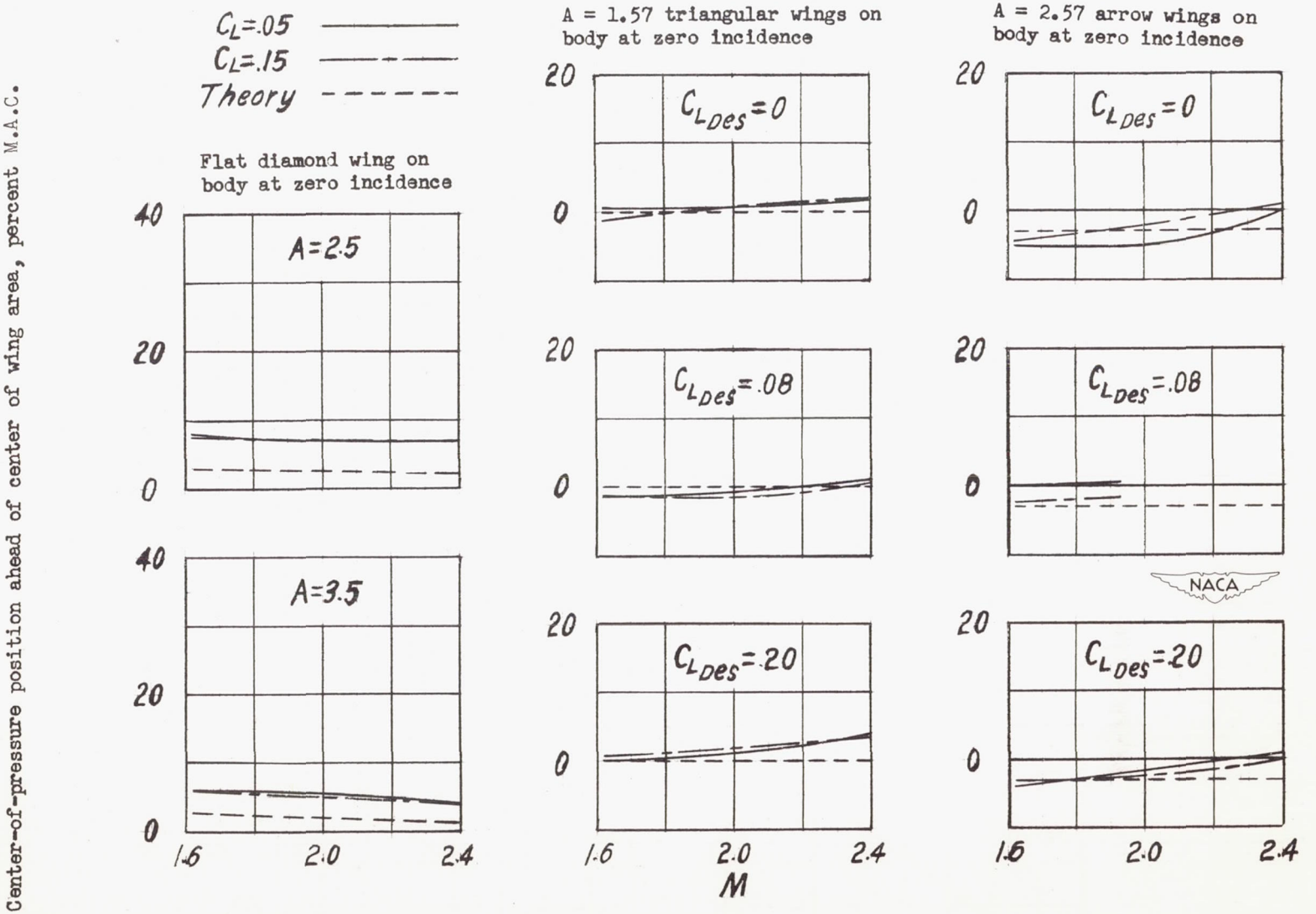

Figure 24.- Variation of center-of-pressure position of various configurations with Mach number and lift coefficient.

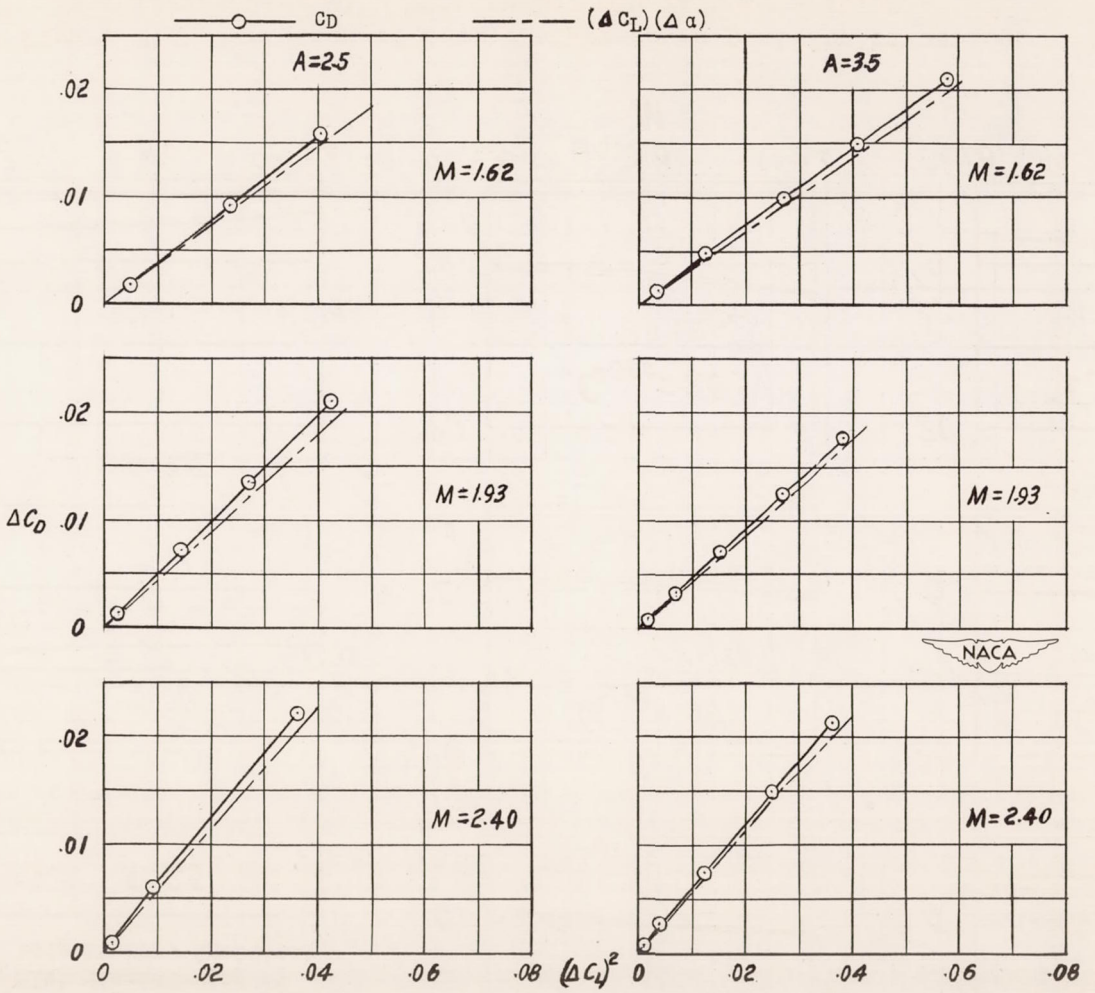

(a) Diamond-wing configurations.

Figure 25.- Variation of ΔC_D with $(\Delta C_L)^2$ of various configurations.

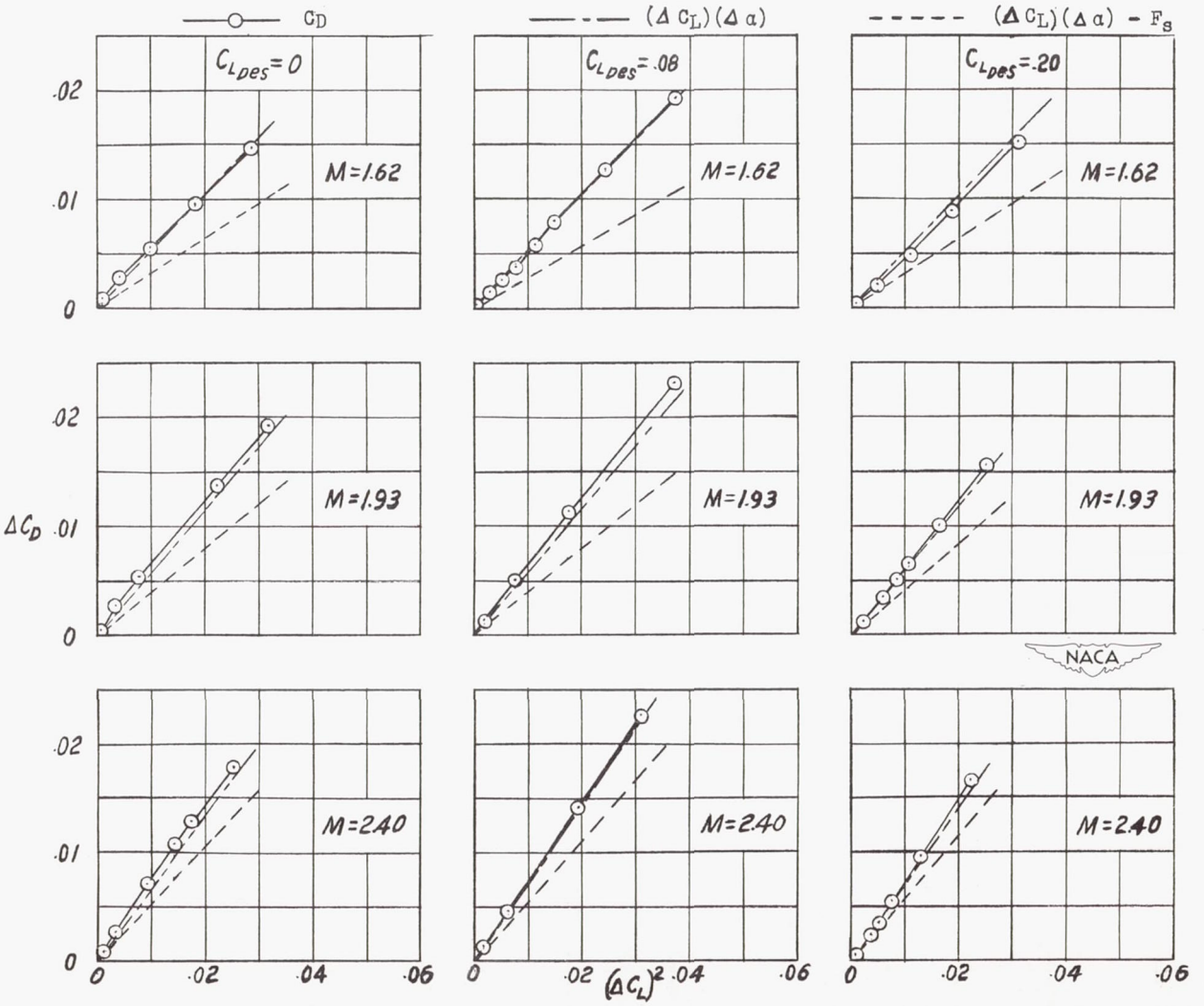

(b) Triangular-wing configurations.

Figure 25.- Continued.

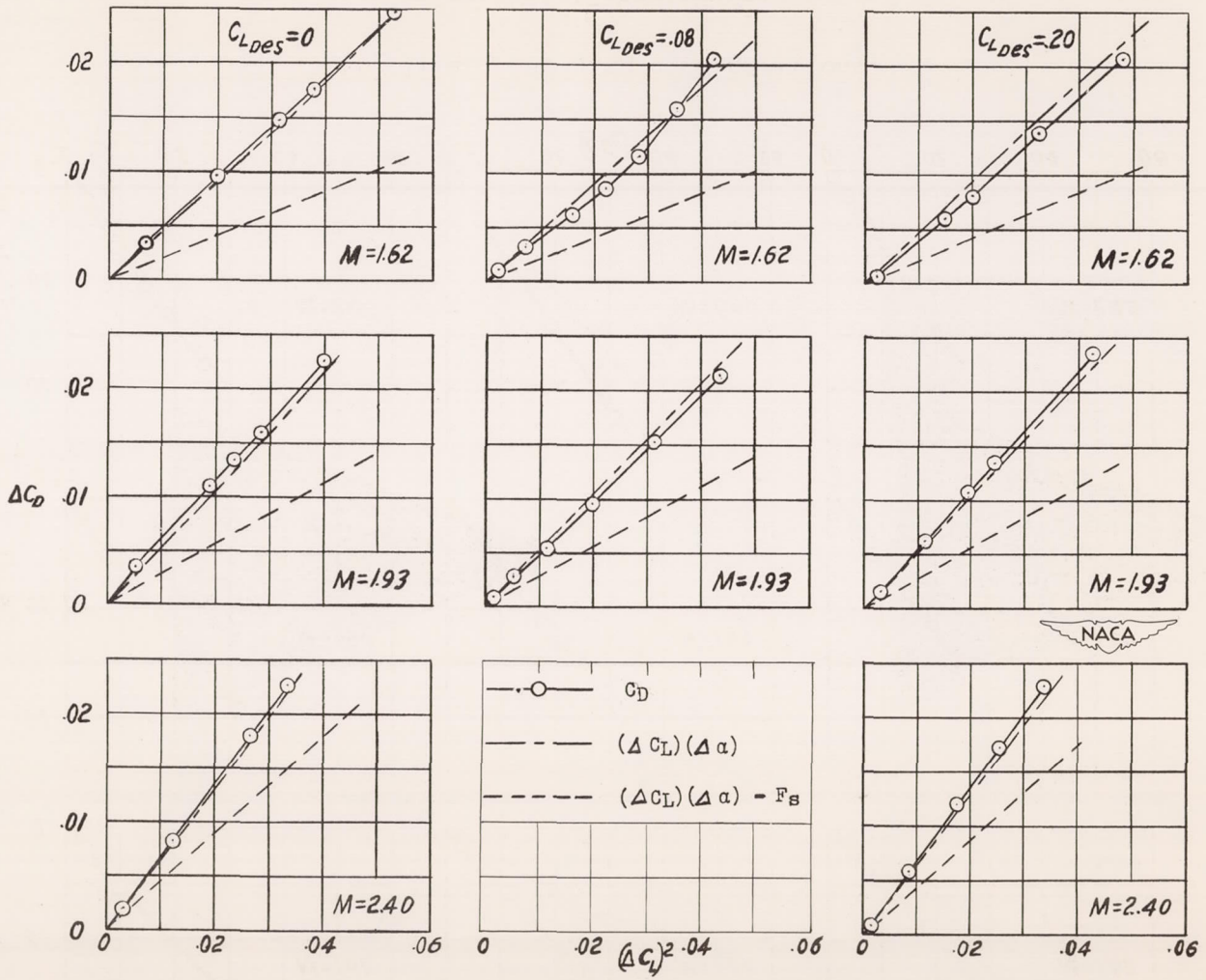

(c) Arrow-wing configurations.

Figure 25.- Concluded.

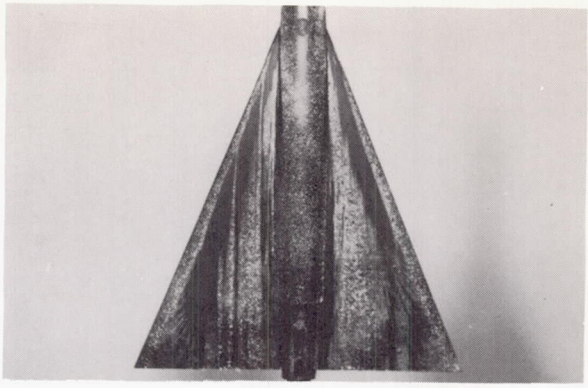

(a) Upper surface.

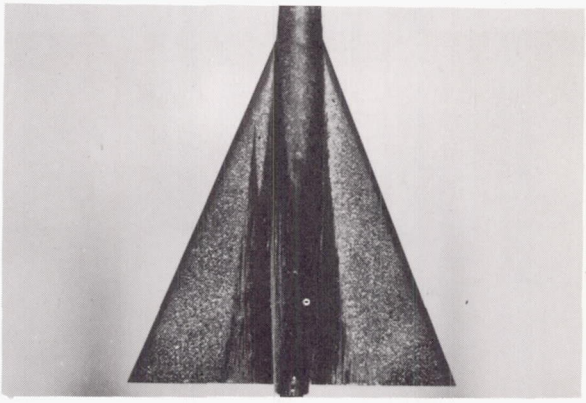

(b) Lower surface.

NACA
L-69135

Figure 26.- Liquid-film pictures of the flat triangular wing on the zero-incidence body at $M = 1.62$ and $\alpha = 4.5^{\circ}$.

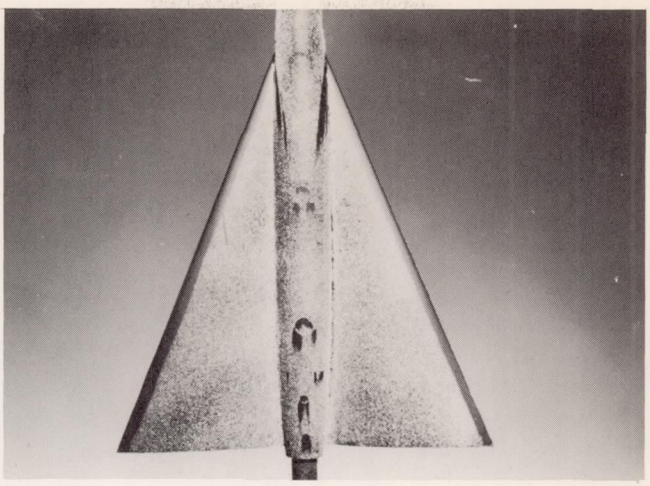

(a) Upper surface.

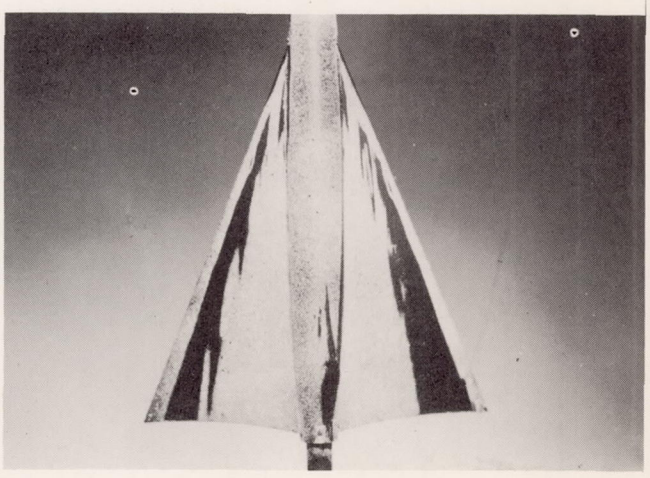

(b) Lower surface.

NACA
L-69136

Figure 27.- Liquid-film pictures of the $C_{L_{Des}} = 0.20$ triangular wing on body at 0° incidence at $M = 1.62$ at $\alpha_{D_{min}}$.

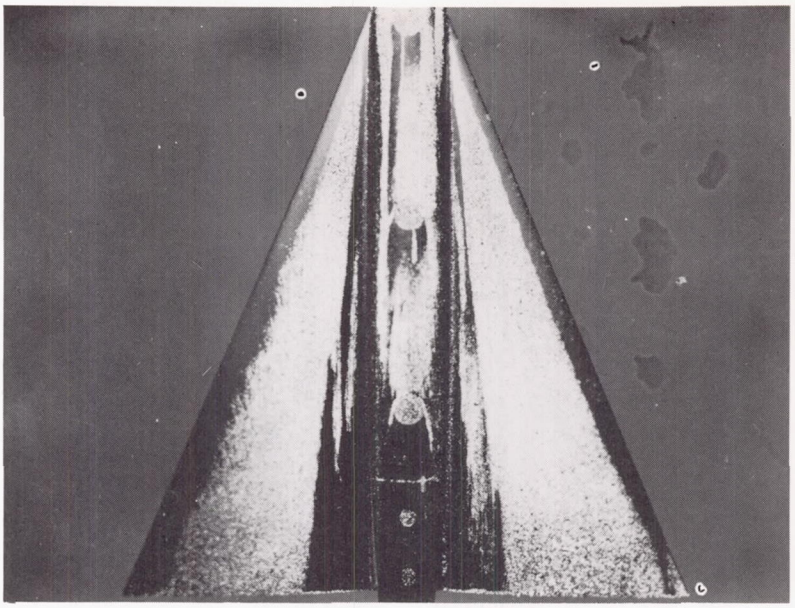

(a) Upper surface.

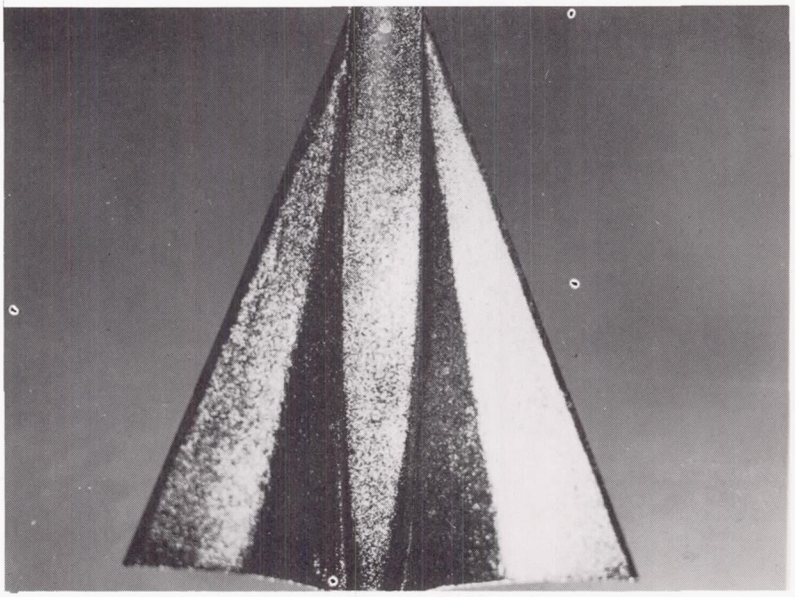

(b) Lower surface.

NACA

L-69137

Figure 28.- Liquid-film pictures of the $C_{L_{Des}} = 0.20$ triangular wing on the zero-incidence body at $M = 1.62$ and $\alpha = 6.8^{\circ}$.

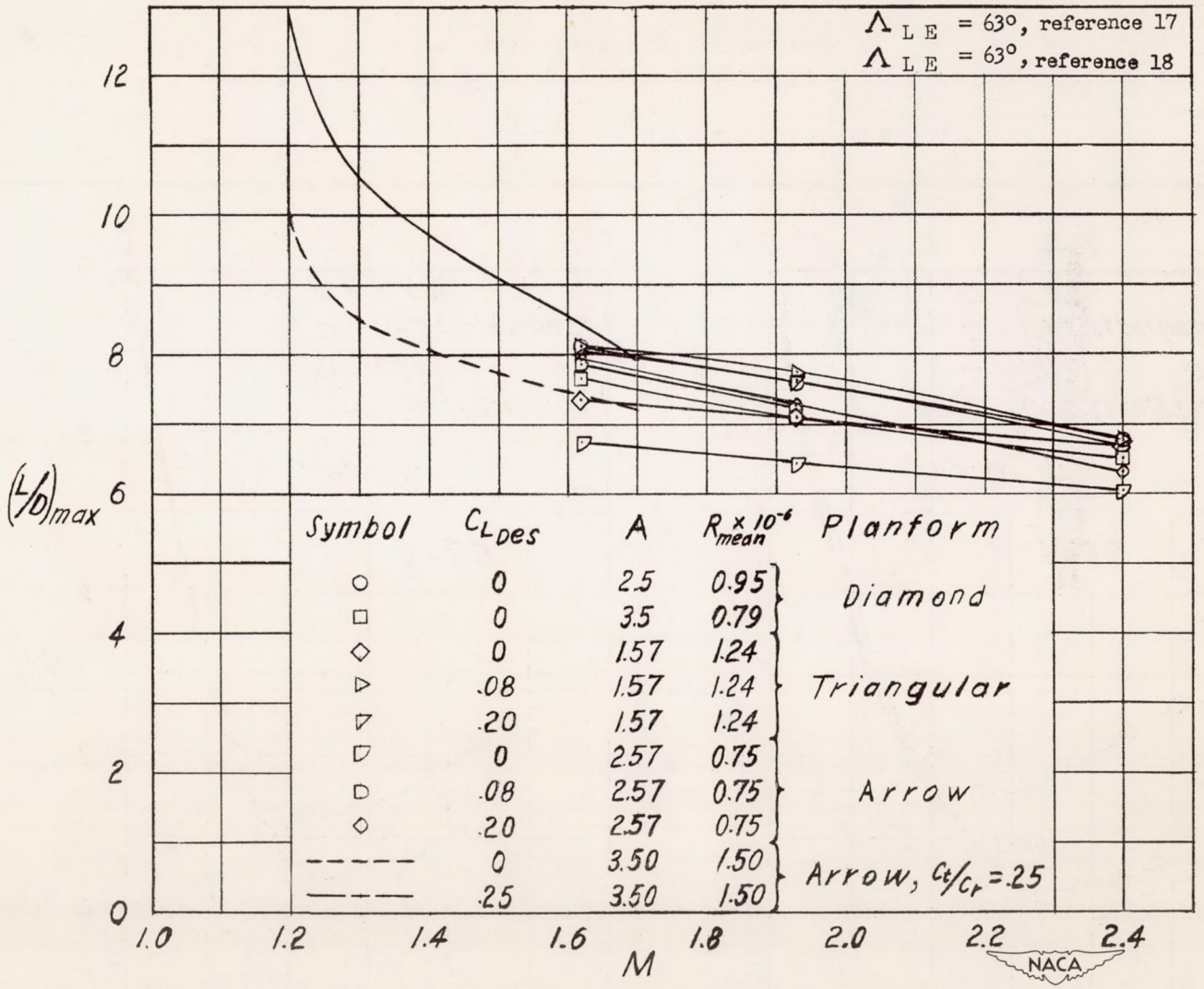

Figure 29.- Summary of the experimental maximum lift-drag ratios of various configurations.

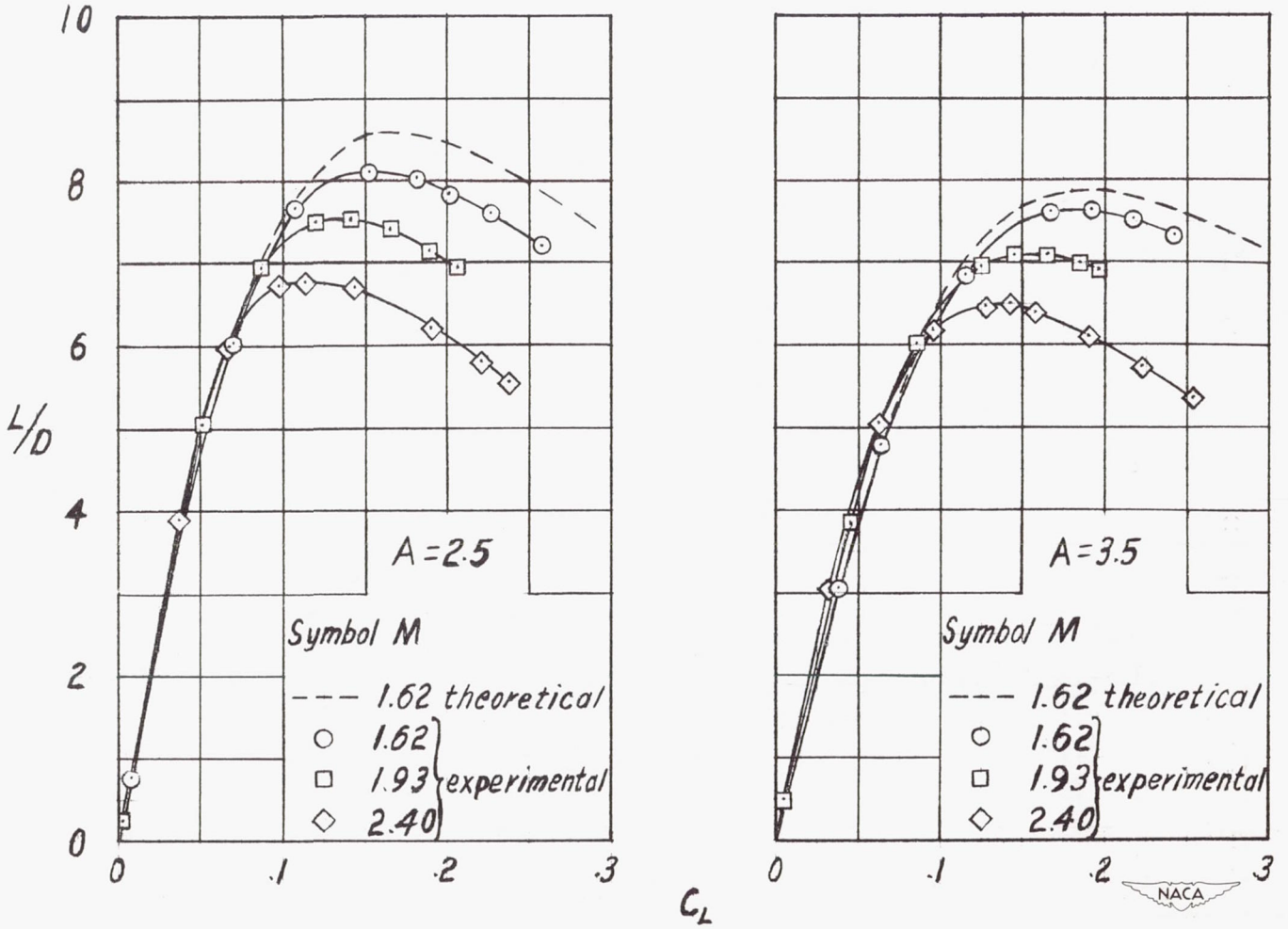

(a) Diamond-wing configurations.

Figure 30.- Variation of the lift-drag ratio with lift coefficient of various configurations.

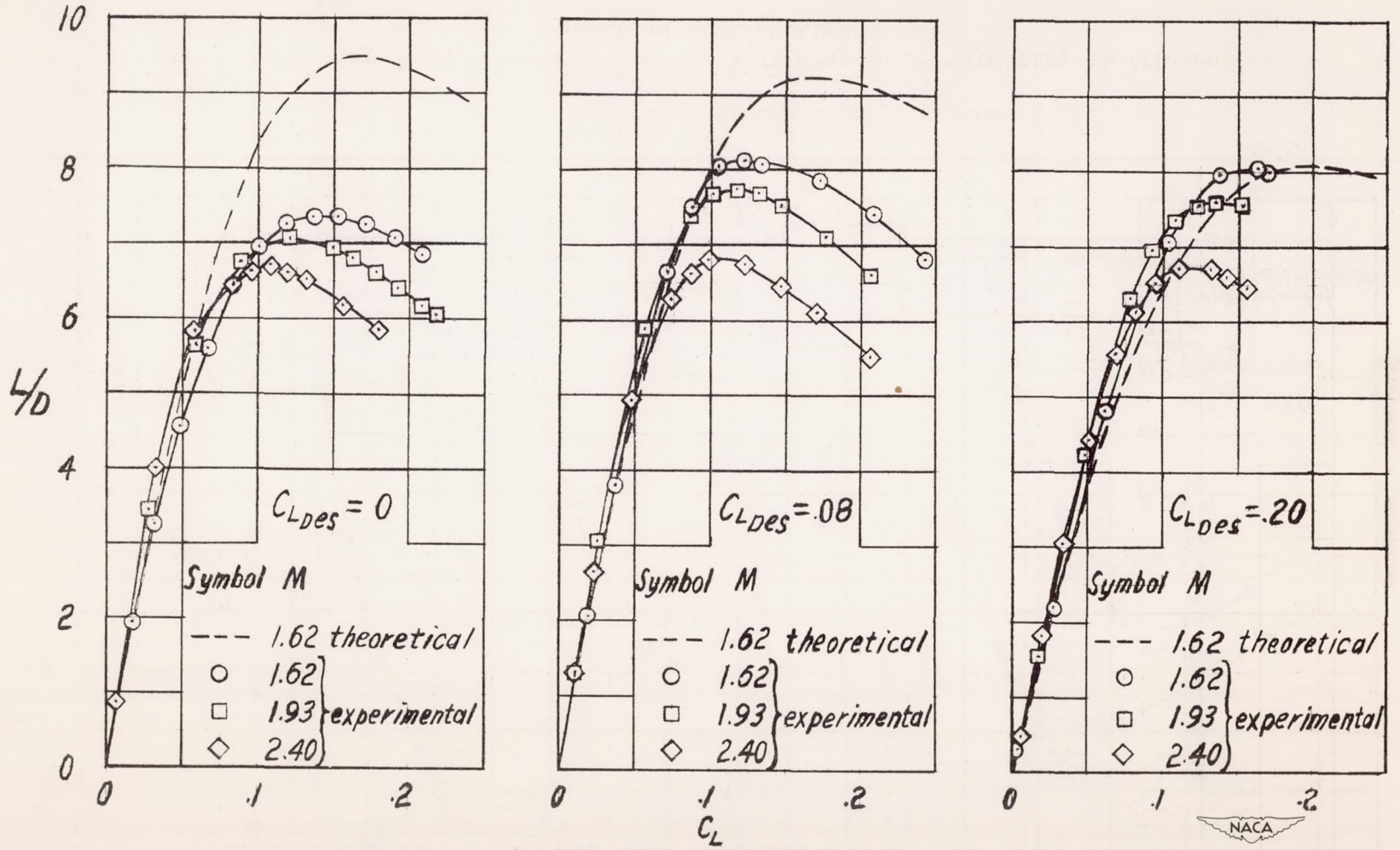

(b) Triangular-wing configurations.

Figure 30.- Continued.

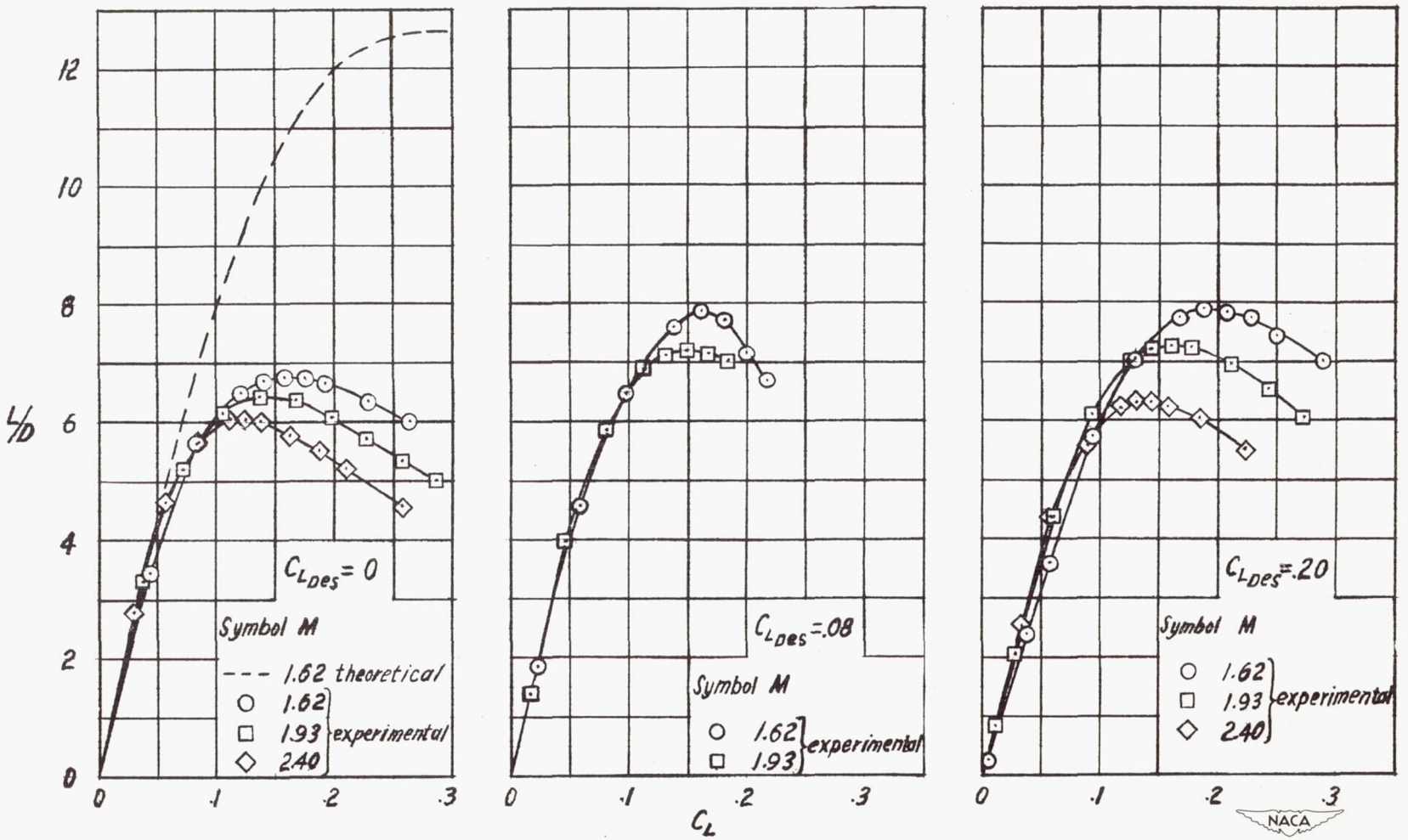

(c) Arrow-wing configurations.

Figure 30.- Concluded.

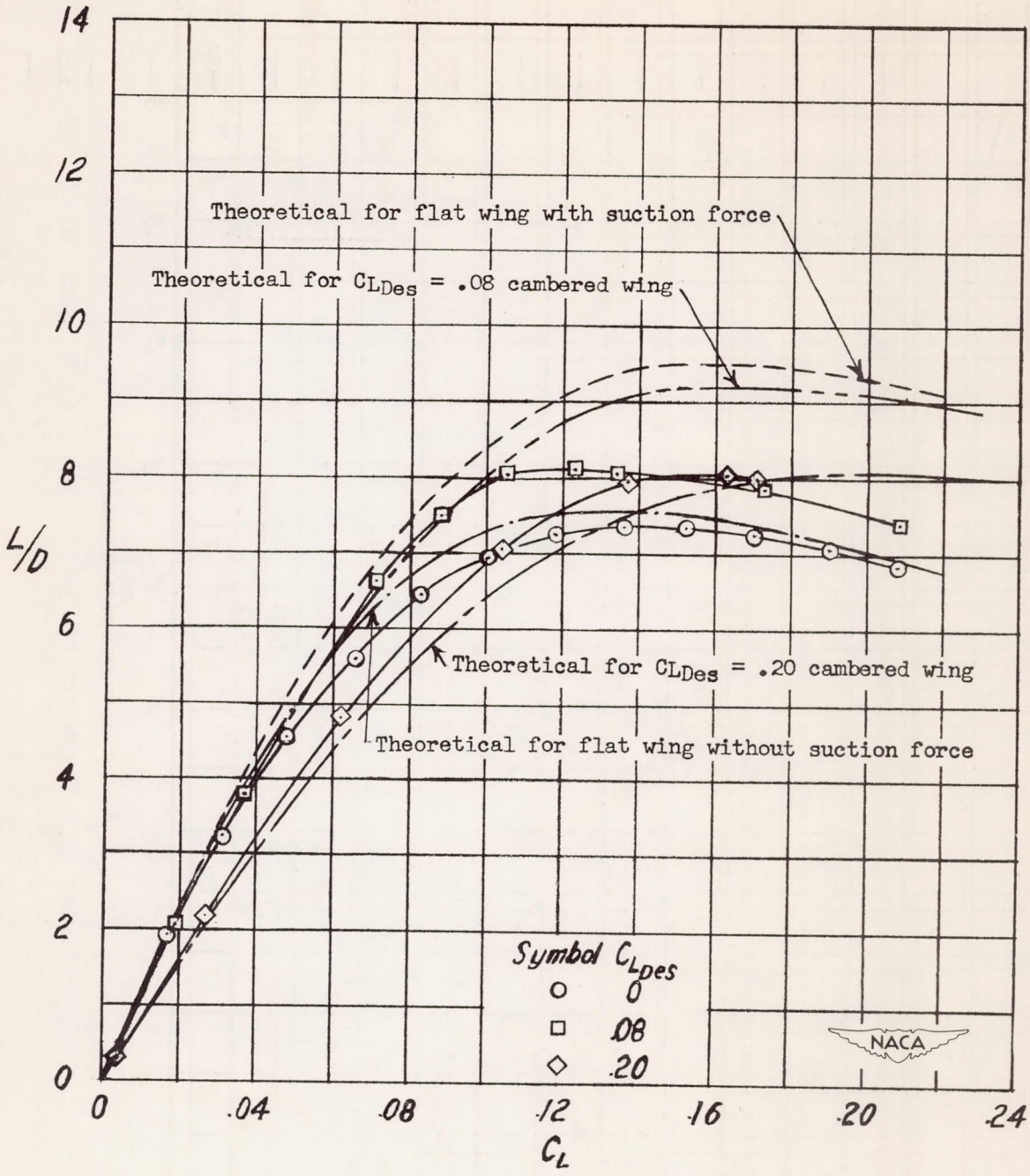

Figure 31.- Thoeretical and experimental variation of the lift-drag ratio with lift coefficient of the triangular-wing configurations at M = 1.62.

Figure 32.- Variation of the function K_3/β with m.

NACA - Langley Field, Va.